1 # A non-genetic model of vascular shunts informs on the cellular
2 # mechanisms of formation and resolution of arteriovenous
3 # malformations

4

5 Marie Ouarné[1][*][†][#], Andreia Pena[1][†], Daniela Ramalho[1][†], Nadine V. Conchinha[1], Tiago
6 Costa[1], Ana Figueiredo[1], Marta Pimentel Saraiva[1], Yulia Carvalho[1], Lenka Henao
7 Misikova[1,2], S. Paul Oh[3], Cláudio A. Franco[1,2][#]

8

9 Affiliations
10 [1]Instituto de Medicina Molecular João Lobo Antunes, Faculdade de Medicina,
11 Universidade de Lisboa, Lisbon, Portugal
12 [2]Universidade Católica Portuguesa, Católica Medical School, Católica Biomedical
13 Research Centre, Lisbon, Portugal
14 [3]Barrow Aneurysm & AVM Research Center, Department of Translational
15 Neuroscience, Barrow Neurological Institute, Phoenix, AZ, USA
16 *Present address: Univ. Bordeaux, Inserm, UMR1034, Biology of Cardiovascular
17 Diseases, F-33600 Pessac, France
18 [†] Co-fist authors.
19 [#]Corresponding authors:
20 Cláudio A. Franco - cfranco@ucp.pt
21 Marie Ouarné - marie.viguier@inserm.fr

Abstract

Arteriovenous malformations (AVMs), a disorder characterized by direct shunts between arteries and veins, are associated with genetic mutations. However, the mechanisms leading to the transformation of a capillary into a shunt remain unclear and how shunts can be reverted into capillaries is poorly understood. Here, we report that oxygen-induced retinopathy (OIR) protocol leads to the consistent and stereotypical formation of AV shunts in non-genetically altered mice. OIR-induced AV shunts show all the canonical markers of AVMs. Genetic and pharmacological interventions demonstrated that changes in endothelial cell (EC) volume of venous origin (hypertrophic venous cells) are the initiating step promoting AV shunt formation, whilst EC proliferation or migration played minor roles. Inhibition of mTOR pathway prevents pathological increases in EC volume and significantly reduces the formation of AV shunts. Importantly, we demonstrate that ALK1 signaling cell-autonomously regulates EC volume, demonstrating that our discoveries link with hereditary hemorrhagic telangiectasia (HHT)-related AVMs. Finally, we demonstrate that a combination of EC volume control and EC migration is associated with the regression of AV shunts.

We demonstrate that an increase in the EC volume is the key mechanism driving the initial stages of AV shunt formation, leading to asymmetric capillary diameters. Based on our results, we propose a coherent and unifying timeline leading to the fast conversion of a capillary vessel into an AV shunt. Our data advocates for further investigation into the mechanisms regulating EC volume in health and disease as a way to identify therapeutic approaches to prevent and revert AVMs.

Introduction

Arteriovenous malformations (AVMs) form as a consequence of maladaptive organisation of blood vessels. They are defined as abnormal high flow connections between an artery and a vein bypassing the capillary bed[1, 2]. Their characteristics lead to reduced tissue oxygenation and to high risks of haemorrhages and ruptures, which are often fatal when occurring in brain. The majority of brain AVMs are a consequence of sporadic events (~95%), yet familial cases exist (~5%)[2]. A large proportion of sporadic cases have been linked to somatic mutations in genes linked to RAS-MAPK pathway[3,4]. Congenital forms are particularly associated with hereditary haemorrhagic telangiectasia (HHT), a rare autosomal dominant genetic disorder[5, 6]. HHT is caused predominantly by *ACVRL1* and *ENG* mutations[7-9], but can also be associated with mutations on *SMAD4*[10,11] or *GDF2*[12-15].

Recent advances in mouse and zebrafish animal models have provided novel insights into the mechanisms of AVM formation and progression. A common characteristic seems the cellular origin of these vascular malformations, which has been mapped to venous or capillary beds[16-18]. A second common feature is the requirement of blood flow as a driving force for AVM development[19-24]. Yet, despite these recent advances, the cellular and molecular mechanisms leading to AVM formation remain unclear. Several reports have highlighted that excessive EC proliferation is a core feature of BMP loss-of-function (LOF)-related AVM development, and interventions blocking EC proliferation such as VEGF, PI3K, AKT, or mTOR inhibitors can prevent the development of retinal AVMs in HHT mouse models[21,25-27]. In KRAS GOF, ECs showed increased cell size, ectopic sprouting, and migration properties[4,28], and these behaviours were sensitive to MAPK inhibition but not to PI3K inhibition[28]. Alongside, cell shape changes have also been suggested to contribute to AVM development both in mouse and zebrafish models[29,30]. More recently, defective flow-migration coupling, which characterizes the ability of ECs to polarise and migrate against the blood flow direction, has been linked to HHT-like AVM models[17,21,30,31], yet other reports showed no issues with flow-migration coupling[16,32]. Thus, to date, we lack a consensus model for AVM development and progression that could integrate all these observations and that would clarify why sporadic and familial cases develop similar vascular malformations despite arising from mutations impinging on very different signalling

3

77   pathways. Here, we describe a reliable mouse model that forms AV shunts in a very

78   predictable spatiotemporal location. This model does not rely on genetic alterations

79   and it allows the investigation of the cellular mechanisms leading to the formation of

80   AV shunts with very high spatiotemporal resolution. As an additional advantage, this

81   model has the advantage to allow the study of the mechanisms of AV shunt regression,

82   which is of special relevance to identifying new therapeutic approaches. Based on the

83   unique features of this AVM model, we were able to propose a general model for the

84   initiation and resolution of AVMs.

Results

Oxygen-induced retinopathy (OIR) model triggers transient non-genetic AV shunts

OIR is a protocol commonly used to model pathological angiogenesis, mimicking retinopathy of prematurity[33,34]. Briefly, neonatal mouse pups are exposed to hyperoxia promoting vascular regression and generating avascular retinal areas. Pups are then returned to normoxic conditions, leading to excessive and pathological neovascularization of the avascular regions. This response depends on hypoxia-driven expression of the main pro-angiogenic factor VEGFA[35]. Our protocol involves placing mouse pups at postnatal day 8 (P8) in a hyperoxia chamber until P11 (fig.1A), after which pups return to normoxia conditions. The day of return to normoxia is termed Day 0. Remarkably, we noted the rapid emergence of AV shunts in the retinal vascular network (fig.1A, B). AV shunts always form between the juxtaposed arteries and veins in the mouse retina (sup.fig.1A), and along the angiogenic border between the vascularized and avascular zone at the centre of the retina (sup.fig.1A, B). For each visible artery-vein pair, we determined the presence/absence of AV shunt and analysed the proportion of AV shunts per retina formed at specific time points. AV shunts appear starting 2 days (Day 2) after the return to normoxia (fig.1B). AV shunts diameter are variable and have a maximum mean width at Day 3 (sup.fig.1C). Interestingly, AV shunts start regressing at Day 5, and at Day 8/9 very few to none can be detected in retinas (fig.1B). This correlates with a decrease in AV shunt diameter from its peak at Day 3 (sup.fig.1C).

Next, we analysed OIR-induced AV shunts for characteristic features linked to genetically-driven AVMs. We observed that AV shunts are functional and carry substantial blood flow (fig.1C). This high-flow profile is further supported by high αSMA+ and desmin+ mural cell coverage (fig.1D and sup.fig.1D), and weak on NG2+ mural cells (sup.fig.1E). Additionally, high-flow AV shunts are also corroborated by high expression levels of KLF4 (fig.1E), a shear stress-responsive transcription factor[36], which was also described as highly expressed in HHT-associated AVMs[32,37]. Together, these results demonstrate that AV shunts are high-flow vessels that become muscularized, resembling to genetically-driven AVMs. Remarkably, despite these common characteristics, the AV shunts developed in this model are not a consequence

117   of reduced ALK1 signalling. EC nuclei in the AV shunt show normal/higher levels of

118   Smad1 phosphorylation in comparison to capillary vessels (fig.1E), suggestive of

119   ongoing BMP-ALK1 signalling. Overall, we identified and characterised a non-genetic

120   model of AV shunt formation that phenocopies genetically-driven AV shunts. We

121   propose that this model allows investigation of both the formation and the regression

122   of AVMs with high spatiotemporal resolution.

123

124   **Non-genetic AV shunt formation is preceded by the enlargement of venules**

125   Next, we analysed with higher temporal resolution the process of AV shunt formation.

126   As AV shunts arise between Day 1 and Day 2, we collected retinas every 4h from timed

127   animals between 24h and 48h. The first AV shunt start appearing at 32h. Around 36h,

128   almost all retinas present AV shunts, with around 40% of AV segments forming a

129   patent AV shunt (fig.2A and B). This means that in around 8h (from 28h to 36h) a large

130   proportion of capillaries connecting AV segments converted into an AV shunt (fig.2A

131   and B). Thus, we concluded that AV shunt formation is a progressive but rapid process.

132   The speed of this process is similar to what is observed in Alk1-defficient mice, where

133   AV shunts can be observed 24h post Alk1 inactivation[7-9]. To understand how such a

134   quick conversion of capillaries into an AV shunt is possible, we studied the architecture

135   of the vascular network during this time window (24h to 48h). As shunts preferentially

136   develop at the limit between the avascularised and the vascularised area (sup.fig.1A

137   and B), we characterised arteries and veins in this region. Artery and vein diameters

138   show an increase prior to AV shunt formation. Vein and arteries when compared to

139   diameters of vessels from animals at Day 0 immediately collected after the hyperoxia

140   period (0h) (sup.fig.2A and B). At 24h (Day 1), the artery mean diameter is ~121%

141   (mean at Day 0 = 10.2 μm vs Day 1 = 12.5 μm) and the vein diameter is ~163% (mean

142   at Day 0 = 17.5 μm vs Day 1 = 28.5 μm) bigger than Day 0 diameters (sup.fig.2A and

143   B). However, this change was not significant as there was a large variability between

144   animals. This increase in vessel diameter continues over time, and by 32h changes

145   became significant in veins and by 40h in arteries (sup.fig.2B). By 40h, when most of

146   AV shunts have already developed, the artery mean diameter increased by ~166%

147   and the vein diameter by ~224% (sup.fig.2A). Yet, remarkably, these effects were even

148   more pronounced in second order branches of veins. The diameters of vessels

149   connecting to arteries (arterioles) and vessels connecting to veins (venules) increase

150   more markedly before shunt formation, when compare to parent vessels (fig.2C,D and

151   sup.fig.2B). For instance, by 40h, the arteriole mean diameter had increased by ~196%

152   (mean at Day 0 = 7.0 μm vs 40h = 13.7 μm) and the venule diameter by ~290% (mean

153   at Day 0 = 4.5 μm vs 40h = 13.0 μm) (fig.2D and sup.fig.2B). Remarkably, the diameter

154   of the first venule was already fully enlarged at 24h, maintaining a stable vessel width

155   over time, whilst the other venules and arterioles increase gradually and peak at 32-

156   40h post-normoxia (fig.2C, D and sup.fig.2B). Given that AV shunts tend to form at the

157   first venous connection (sup.fig.1B), these results suggest that structural adaption of

158   the first venules precedes AV shunt formation. Given that blood flow is required for

159   AVM formation[19,20,22,23,38], we hypothesise that OIR-dependent venule diameter

160   increase predisposes capillary vessels to develop AV shunts by promoting unregulated

161   blood flow between high-flow segments (proximal arteries and veins). To investigate

162   this hypothesis, we next focused on the cellular mechanism leading to venule diameter

163   increase at Day 1.

164

Endothelial proliferation nor endothelial migration are involved in OIR-induced AV shunt formation

167   First, we investigated EC proliferation, as it has been linked to AVM formation

168   previously[21,25-27], and that the OIR model is associated with neo-angiogenesis and

169   extensive EC proliferation[34]. Indeed, we observed extensive EC proliferation in the

170   different vessel beds prior to shunt formation, assessed by The fraction of EdU+ or

171   pHH3+ ECs (fig.3A and B, sup.fig.3A and B). In order to assess the involvement of EC

172   proliferation in AV shunt formation, we blocked cell proliferation using mitomycin C, a

173   drug that inhibits DNA synthesis and cross-links DNA, effectively blocking cell cycle[39].

174   We treated pups with mitomycin C either at 0h or at 24h post-normoxia and collected

175   retinas at Day 3 (fig.3C). Immunofluorescence for pHH3 or EdU demonstrates efficient

176   abrogation of EC proliferation in mitomycin C-treated animals (fig.3C, sup.fig.3A-C).

177   Accordingly, we observed a decrease in EC density in all vascular beds, including AV

178   shunts, in mitomycin C-treated animals when compared to PBS-treated mice

179   (sup.fig.3C). Yet, surprisingly, we observed no differences in the occurrence of AV

180   shunts between PBS-treated and the mitomycin C-treated pups (fig.3D), nor a

181 difference in shunt diameter between the two groups (fig.3E). Thus, we concluded that

182 EC proliferation is not required for AV shunt formation or growth in our model.

183 Next, we explored the role of EC migration in AV shunt development. Flow-migration

184 coupling has been described as a player of AVM formation[17,21]. We analysed flow-

185 migration coupling using the EC front-rear polarity GNRep mouse strain[40] (sup.fig.4A-

186 D). We found that at Day 0 there was a non-significant reduction in terms of polarity

187 patterns between staged non-OIR animals (P13) and Day 0, suggesting that the OIR

188 protocol does not affect significantly polarity patterns in arteries and veins (sup.fig.4B).

189 Interestingly, rather than a decrease in polarity, we found a significant increase in the

190 polarization patterns of ECs in arteries or veins, between Day 1 and Day 2, the period

191 where AV shunts develop (sup.fig.4B). In addition, ECs in AV shunts also showed a

192 significant polarization against the flow direction (sup.fig.4C and D). Overall, these

193 results suggest that flow-migration coupling is not the main mechanism leading to the

194 formation of OIR-induced AV shunts.

195 Next, we evaluated the contribution of EC migration in our model. We first used the

196 endothelial-specific conditional KO of Arpc4 (*Arpc4*-iECKO) mouse line. Arpc4 is an

197 essential subunit of the Arp2/3 complex, which creates branching actin networks that

198 are fundamental for cell migration[41]. We previously demonstrated that Arpc4-deficient

199 ECs showed impaired cell motility, efficiently blocking EC sprouting and EC migration

200 in the mouse retina[41]. To avoid confounding effects, we induced *Arpc4* deletion,

201 through tamoxifen injection, during the hyperoxia stage and collected retinas at Day 3

202 (fig.3F). As expected, *Arpc4* endothelial-specific deletion decreases the number of

203 neo-angiogenic vascular sprouts during the revascularization stage (sup.fig.4E),

204 consistent with the essential role of Arp2/3 complex in cell migration and invasion[41].

205 Remarkably, inhibition of cell motility led to a small, but significant, reduction in the ratio

206 of AV shunt formation at D3 (fig.3G). Yet, inhibition of the Arp2/3 complex did not affect

207 the diameter of existent AV shunts (fig.3H). To further confirm these results, we

208 additionally targeted SRF in ECs. Alongside Arp2/3 complex, SRF is essential for EC

209 migration, tip cell invasion and vessel development[42-44]. We used a similar protocol to

210 inhibit SRF in ECs as for Arpc4, using the *Srf*-iECKO mouse line. Consistently, *Srf*

211 endothelial-specific deletion decreased the number of neo-angiogenic vascular

212 sprouts during the revascularization stage (sup.fig.4F). Yet, contrary to Arp2/3 complex

213   inhibition, we did not observe a signifcant reduction in the percentage of AV shunts

214   being formed at Day 3 in *Srf*-iECKO animals (fig.3I and sup.fig.4G). In addition, *Srf*

215   endothelial deletion significantly decreased the diameter of AV shunts (sup.fig.4H),

216   suggesting additional effects besides inhibition of cell migration.

217   Altogether, these combined results indicate that EC migration may contribute but it is

218   not essential for AV shunt formation or development.

219

220   **EC volume changes drive AV shunt formation**

221   Given that neither cell migration nor cell proliferation played major roles in AV shunt

222   formation, we hypothesise that imbalances in EC distribution may cause enlargements

223   of vessels. To examine this aspect, we decided to analyse cell density between Day 0

224   and Day 1 in different vascular beds, at a period preceding AV shunt formation. Within

225   this time window, all vessel beds increase their diameters, with the first venule

226   connection showing the highest increase in vessel diameter (fig.2D and sup.fig.2B).

227   We quantified the number of ECs per vessel area in different vessel segments to

228   determine local EC density (fig.4A, B and sup.fig.5A). Interestingly, the increase in

229   vessel diameter in arteries, veins and capillaries (either on the arterial or venous side)

230   correlated with a significant decrease in EC density (fig.4B). Remarkably, this effect

231   was particularly strong in capillaries connecting to veins (fig.4B and sup.fig.5A). These

232   observations suggest that the increase in vessel diameters is likely a consequence of

233   cell volume changes rather than an increase in the number or redistribution of ECs,

234   through proliferation or migration. This hypothesis fits with the low impact of inhibition

235   of proliferation or cell migration on AV shunt formation (fig.3). To assess if the cell

236   volume increases prior to shunt formation, we stochastically activated Cre

237   recombinase, using a low dose of tamoxifen, to promote the expression of membrane-

238   bound GFP in retinal ECs, and analysed cell shape and cell volume at the single-cell

239   level. For this, we crossed the R26-mTmG mouse line with the Cdh5-CreERT[2] line[45,46],

240   and we used previously established protocols[42,47,48]. We segmented the membrane

241   GFP signal to generate a solid object and we analysed cell morphology and measured

242   the total volume for each object (sup.video1). Regarding cell shapes, no significant

243   changes in the morphology of cells could be observed, with Day 1 cells displaying

244   similar shapes to Day 0 cells (fig.4C). Remarkably, we observed a significant increase

245   in cell volume for ECs in all vascular beds at Day 1 (fig.4C, D and sup.fig.6A).

246   Remarkably, the increase in cell volume is much more prominent on the venous side

247   (~200% increase; Day 0 mean = 1123 μm^3 to Day 1 mean = 2332 μm^3 for veins and

248   Day 0 mean = 1210 μm^3 to Day 1 mean = 2332 μm^3 for venous capillaries) than on the

249   arterial side (~125% increase; Day 0 mean = 946 μm^3 to Day 1 mean = 1227 μm^3 for

250   arteries and Day 0 mean = 1062 μm^3 to Day 1 mean = 1390 μm^3 for arterial capillaries)

251   of the vascular tree (fig.4D and sup.fig.6A). This effect was not due to abnormal EC

252   volume at Day 0, as cell volumes are equivalent between cells from Day 0 and non-

253   OIR retinas in any of the vascular beds (sup.fig.6B). This effect correlates well with the

254   bigger increase in vessel diameter on the venous side (fig.2D and sup.fig.2A).

255   Collectively, these results point in favour that the initiation of AV shunt formation stems

256   from an increase in EC volume on the venous side.

257   To confirm this hypothesis, we used pharmacological inhibitors to block key metabolic

258   pathways known to be involved in angiogenesis and control of cell volume. First, we

259   targeted glucose, as angiogenic ECs use glycolysis as the main source of energy[49].

260   To do so, we use 2-deoxy-D-glucose (2-DG), which acts as a competitive substrate for

261   hexokinase, inhibiting ATP production from glucose[50]. Remarkably, no significant

262   changes in AV shunt formation or AV shunt diameter were observed (sup.fig.6C-E).

263   Next, we used an inhibitor of PFKFB3 (3PO), a key glycolytic enzyme, which was

264   identified as being critical to vessel formation and a regulator of tip and stalk cell

265   behaviour[51]. Similar to 2-DG treatment, we observed no significant changes in AV

266   shunt formation or AV shunt diameter were observed (sup.fig.6C-E). Thus, we

267   concluded that glycolysis does not regulate AV shunt formation. Next, we tested the

268   inhibition of the mammalian target of rapamycin (mTOR), a key protein complex

269   regulating cell metabolism, cell growth and cell proliferation[52]. We used everolimus,

270   which preferentially targets mTOR complex 1 (mTORC1). Also, mTOR inhibitors were

271   previously shown to prevent AVM in a mouse model of HHT[27]. A single dose of

272   everolimus at Day 0 significantly decreased EC volume at Day 1, normalizing it to

273   volumes similar to Day 0 cells. Daily injections of everolimus between Day 0 and Day

274   2 maintained normalization of EC volumes at Day 3 (fig.5A and B). Importantly,

275   everolimus-induced normalization of EC cell volumes correlated with a significantly

276   decreased in the rate of AV shunt development at Day 3 (fig.5C and D), alongside a

significant decrease in shunt diameter (fig.5E), suggesting that a change in EC volume is an essential step initiating AV shunt formation in our mouse model.

Taken together, our results collectively suggest a model describing the formation of an AV shunt (fig.6A). We propose that AV shunts originate from the abnormal and asymmetric enlargement of venous vessels due to an increase in EC volume as the main cellular mechanism. This asymmetric vessel enlargement promotes unregulated flow rates in the proximal capillary bed connected to high-flow arteries and veins, which correlates with the interface with the avascular zone in the OIR model. This initial uncontrolled flow pattern self-amplifies by the conversion of a capillary vessel path into a proper AV shunt. These later events will likely involve EC migration and EC proliferation, in addition to EC volume changes.

To test if the proposed model applies to genetic models of AVMs, we focused on *Alk1* LOF in ECs. Endothelial-specific deletion of *Alk1* leads to rapid (30h-36h) development of AV shunts in the mouse retina[24,53]. Concordant with our data on OIR-induced AV shunts, we observed a significant increase in vessel diameter at 24h post-recombination, a stage prior to AV shunt formation (fig.6B). This increase was more robust on the venous side, when compared to the arterial side, further corroborating the data obtained on the OIR model (fig.6B). Next, to confirm if vessel diameter increase was associated with changes in cell volume, we intercrossed the Alk1 mouse model with the R26-mTmG mouse line. Low-dose tamoxifen injection allows recombination of a few ECs (sup.fig.6F), enabling the measurement of Alk1 LOF in cell volume in the context of a WT retina (fig.6C), without generating AV shunts. Strikingly, stochastic recombination of Alk1 leads to a significant increase in EC volume at 24h post-recombination specifically in the venous regions, whilst the arterial ECs showed no significant changes (fig.6C and D). Thus, we concluded that Alk1 signalling controls EC volume in a cell-autonomous manner and that the initiation steps driving AV shunt formation share similarities between HHT-induced and OIR-induced models. This suggests that EC volume control, and concomitant flow pattern deregulation, is a key mechanistic step leading to AVM development in HHT.

AV shunt regression is dependent on endothelial flow-migration coupling and cell volume changes but not on EC apoptosis

AV shunt regression is of particular clinical relevance yet very little is known about the underlying cellular and molecular mechanisms. Thus, we took advantage that OIR-induced AV shunts are not stable to investigate how AV shunts resolve. AV shunts start regressing at D5, and by D8 no AV shunts can be detected (fig.1B). We hypothesise that shunt resolution could be the outcome of one or a combination of several mechanisms, including EC apoptosis, cell migration or cell volume changes.

First, we investigated apoptosis, which could lead to a reduction in the number of ECs in a vessel segment leading to a decrease in its diameter. Active-caspase 3 staining during the resolution phase highlights the existence of very few apoptotic ECs during this stage (sup.fig.7A), and thus we excluded apoptosis as a mechanism for AV shunt resolution.

Next, we evaluated if cell dispersion through cell migration could explain AV shunt resolution. During this stage, we observed that shunt regression coincides with the neo-vascularization of the avascular area (fig.7A and B). This leads to an increase in the number of connections between the AV shunt and the parent arteries and veins and an increase in the vascular density of the neo-capillary network (fig.7A, B and sup.fig.7B). Given that flow-migration coupling is essential for vascular remodelling and network optimisation[54-57], we hypothesise that redistribution of blood flow through the new vascular segments could reroute EC migration paths. This may decrease the number of ECs moving into AV shunts, and therefore contribute to their normalisation. As the majority of neo-vessels connect AV shunts with the adjacent veins (fig.7A and B), we predicted that this region may show the first signs of AV shunt normalisation. To validate this hypothesis, we first assessed vascular perfusion of neo-vascular networks using intracardiac lectin injections. We observed a significant increase in the number of perfused vessel branches from both the vein and the AV shunt, from Day 2 to Day 6 (fig.7C and D), suggesting progressive blood flow redistribution from AV shunts towards newly formed vascular beds. This coincided with an increase in the overall perfusion of the neovascular area (sup.fig.7C). AV shunts start thinning and become less discernible at the venous side (fig.7A and C), where the connection between the AV shunt and the draining vein becomes more entangled. Remarkably,

339 quantification of AV shunt diameters from the arterial and venous sides showed a

340 preferential decrease in diameter from the venous side starting at Day 4, which

341 precedes AV shunt regression (fig.7E). Overall, these results strongly suggest that AV

342 shunt regress due to changes in flow distribution and EC rerouting, occurring first on

343 the venous side.

344 To tackle the importance of the blood flow redistribution and EC migration-flow coupling

345 in AV shunt regression, we took advantage of the *Arpc4*-iECKO and *Srf*-iECKO mouse

346 models to inhibit EC migration and invasion. To avoid any impact on the formation of

347 AV shunts, we induced *Arpc4* or *Srf* deletion after return to normoxia. As expected,

348 *Arpc4*-iECKO pups showed a significant reduction in the neo-angiogenic sprouts and

349 a significant reduction in the vascularization of the avascular region (sup.fig.6D and E).

350 Remarkably, at Day 7, *Arpc4*-iECKO pups preserved AV shunts, contrary to control

351 pups, where AV shunts almost completely regressed (fig.8A and B). A similar trend

352 was found when inhibiting SRF function in ECs. *Srf*-iECKO pups also showed a

353 significant reduction in the number of neo-angiogenic sprouts (sup.fig.7F), alongside

354 the maintenance of AV shunts at Day 9 (fig.8C and D). Altogether, we concluded that

355 formation of a neo-vascular network is essential for AV shunt regression.

356 Finally, we analysed EC volume. Given that an increase in EC volume is the driving

357 force for AV shunt formation (fig.4 and 5), we examined if the regression of AV shunts

358 could correlate with a decrease in EC volume. To do so, we employed a similar

359 approach as for AV shunt formation, but we induced stochastic recombination of the

360 reporter line at Day 0 instead. The analysis of ECs in each vascular bed demonstrated

361 normalization of cell volume in arterial and venous cells, obtaining volumes

362 comparable to Day 0 (fig.8E). Thus, taken together, our data points towards a model

363 where AV shunts resolve by a combination of EC dispersion through flow-migration

364 coupling and EC volume normalization (fig.8F). Both mechanisms may cooperatively

365 promote the reversion of abnormally formed AV shunts into capillary vessels of normal

366 diameter.

367

368

Discussion

In this work, we unravelled a new non-genetic mouse model to study AV shunt formation and regression with high spatiotemporal resolution. Through genetic and pharmacological interventions, we mechanistically demonstrated that EC volume control, rather than EC proliferation, is a key step in the formation of AV shunts, whilst a combination of cell volume control and EC flow-migration coupling is associated with the regression of these vascular malformations.

Based on our results, we propose a coherent and unifying timeline leading to the fast (24h) conversion of a capillary vessel into an AV shunt. A first trigger, either genetic mutation or specific environmental conditions, leads to a substantial increase in the volume of ECs and a concomitant increase in vessel calibre. Remarkably, our detailed analysis showed that the early changes driving both AV shunt development and regression are preferentially located in the venous compartment (veins and venous capillaries). This is in agreement with previous studies on HHT-associated AVMs that pointed towards ECs in capillaries or veins as the main cellular origin of vascular shunts[16-18,21]. This increase in cell volume is fuelled, at least partially, via the mTOR pathway, and it leads to the expansion of the capillary diameter. In turn, the expansion in vessel diameter decreases flow resistance leading to an increase in flow rates in the vessels prone to be converted into shunts. Increased levels of blood flow through these dilated vessels further expand the vessel lumen through a combination of EC migration, flow-migration coupling and EC proliferation. Recruitment or transdifferentiation of mural cells promotes the consolidation of the high-flow shunt. In addition, we showed that AV shunts can gradually regress through a combination of flow-migration coupling-induced remodelling and cell volume changes. The regression relies on the intrinsic capacity of ECs to migrate and rearrange within the vascular network in order to resolve maladaptive vessel configurations, an essential behaviour that we refer to as vascular plasticity[57]. In this context, the establishment of new vessel connections, which create new flow routes is a prerequisite for AV shunt regression, and blockage of vascular plasticity can sustain environmentally-driven AV shunts.

This detailed description of the initial steps in the formation and resolution of AVMs raises further questions. What is the relative contribution of EC volume control in shunt regression in relation to EC migration and EC redistribution? A large contribution of EC

volume normalization would point towards a common cellular process involved in the genesis and resolution of these vascular anomalies, whilst a low contribution would indicate fundamentally different mechanisms of the two biological phenomena. The latter could indicate that known mutations driving AV shunts may impair two distinct cellular processes, one leading to EC volume increases and another disrupting vascular plasticity, which will promote the formation and, at the same time, prevent the mechanisms of regression.

One additional key question resides in the molecular mechanisms of EC volume control. So far, this question has raised very limited attention in the field of vascular biology. Yet, previous connections between cell size have been reported to be associated with AVM formation. For instance, HHT-driven mutations have been shown to lead to bigger EC sizes in zebrafish and mice[29,30]. Moreover, KRAS-activating mutations have recently been identified as the main driver of sporadic brain AVMs and they were also associated with increases in EC volume[4,28]. However, constitutively active Notch4 also gives rise to AVMs with increased capillary diameters, yet cell volume changes have not been reported so far[22,38,58]. How these pathways regulate cell volume remains to be elucidated. Generally, short timescale cell volume control is achieved through osmolarity control, mainly via ion channels[59,60]. Longer timescale cell volume control has been mostly studied in the context of cell cycle and has been associated with several pathways promoting anabolism, such as the mTOR pathway[52,61], MYC signalling[62,63], the YAP/TAZ pathway[64-66], and more recently cell mechanics[67,68]. Even if we cannot exclude the impact of osmolarity effects and short timescale fluctuations on cell volume, the significant normalisation of EC volumes upon mTOR pathway inhibition with everolimus treatment (fig.5), and concomitant impact on AV shunt formation, strongly suggests that anabolic activity is a key fundamental step in pathological EC volume control. How AVM-associated pathways regulate anabolism may differ according to the associated mutations. For instance, KRAS activating mutations rely on MEK activity rather than on AKT/PI3K signalling, an upstream regulator of mTOR activity[4,28], whilst ALK1, ENG or SMAD4 LOF mutations showed sensitivity to AKT/PI3K signalling inhibitors[21,25,26]. In this regard, OIR-induced AV shunts are more closely related to HHT-associated lesions rather than to KRAS-induced AVMs. Remarkably, BMP pathway LOF mutations require pro-angiogenic

433   environments to induce AVM formation whilst KRAS activating mutations are able to

434   promote AVM development in quiescent endothelium[24,26,28,69], which further points

435   towards a closer mechanistic relationship between OIR-induced AV shunts with HHT-

436   associated AVMs.

437   Despite the strong evidence of cell volume as a key mechanism driving AVM formation,

438   how EC volume-dependent lumen enlargement feedbacks into flow dysregulation that

439   promotes capillary-to-shunt conversion remains largely obscure. Through a rheological

440   perspective, differential resistance of capillary vessel segments would explain

441   preferential shunting of flow through enlarged vessels, yet vascular cells have evolved

442   numerous mechanisms tightly controlling blood flow, with a particular emphasis on

443   mural cells[70]. Thus, it is likely that additional mechanisms related to mural cell activity

444   may be affected in our model which further promotes AV shunt development.

445   Interestingly, recent reports have also linked mural cell function and AVM formation in

446   animal models[71-73]. Yet, to our perspective, dysfunction of mural cell-dependent flow

447   control is rather a facilitator rather than a driver, and pre-requires an imbalance in EC

448   volume as an initiating step.

449

450   Finally, our work also establishes a solid model to investigate AVM regression. How

451   and why genetically driven AVMs do not regress is a key open question. Recently,

452   thalidomide treatment has shown promising effects on the regression of AVMs in

453   patients with a severely symptomatic AVM that is refractory to conventional

454   therapies[74,75]. Yet, the molecular mechanisms of the action of this broad-spectrum drug

455   remain unclear. Taking our results into consideration, we can propose that thalidomide

456   may either promote cell volume normalization and/or efficient flow-migration coupling-

457   induced remodelling.

458   Moreover, our novel insights into AV shunt regression also open the perspective of a

459   novel class of mutations that might be associated with human AVMs. As AV shunts

460   can naturally occur in genetically-competent individuals, mutations impacting AV shunt

461   resolution mechanisms, rather than AV shunt formation mechanisms, could promote

462   the stabilisation and growth of those lesions by a lack of capacity to resolve them.

463   Given that mutations in Srf and Arp2/3 complex limit new sprout formation and AV

464   shunt regression, we predict that mutations impacting EC motility and sprouting when

465   associated with naturally occurring shunts may lead to AVMs.

466

467   In conclusion, we demonstrated that EC volume is the key mechanism driving AVM

468   formation, and it seems transversal to genetic and non-genetic AVM mouse models.

469   Our data strongly underline the necessity to further investigate the mechanisms

470   regulating EC volume in health and disease as a way to identify therapeutic

471   approaches to prevent and revert AVMs.

Materials and methods

Mice

All animal experiments carried out in this work were performed in compliance with the relevant laws and guidelines that apply to the Instituto de Medicina Molecular (iMM) – João Lobo Antunes, Faculty of Medicine, University of Lisbon, Portugal. Animal procedures were performed under the Direção-Geral da Alimentação e Veterinária (DGAV) project licenses 012092/2016 and 017722/2021.

Mice were maintained at the Instituto de Medicina Molecular (iMM) under standard husbandry conditions (under specific pathogen-free conditions and kept in individually ventilated cages) and under national regulations.

The following transgenic mouse strains were used in this study: GNrep[40], *Arpc4* floxed[76], *Srf* floxed[77], *Alk1* floxed[24], and R26-mTmG[45] mice. The different strains were crossed with Cdh5(PAC)-CreERT2 strain[46] or Pdgfb-CreERT[78] to obtain the desired genotypes. Cre-negative littermates were used as controls in KO strain experiments. Both males and females were used, without distinction. Animals were sacrificed at different endpoints and the eyeballs were collected.

Treatments

4-hydroxytamoxifen (H6278, Sigma-Aldrich) was injected intraperitoneally (IP) (20 µg/g) at different ages depending on the mouse strain and studied AV shunt stage. KO strains were injected at post-natal day 8 (P8) and P10 to study AV shunt formation or at Day 1 (P12) and Day 2 (P13) to study AV shunt resolution. GNrep mice were injected at P1 and P3 to trigger reporter expression. To trigger mosaic recombination in R26mTmG, a low dose of 4-hydroxytamoxifen (0.4 µg/g) was injected IP only once at P8 or P14. Non-OIR pups were injected with the same low dose of 4-hydroxytamoxifen tamoxifen three days before the day of collection.

To block cell proliferation during shunt formation, mitomycin C (SC-3514B, ChemCruz) was injected IP (10 µg/g) at Day 0 or Day 1 and pups were collected at Day 3. PBS was injected in control pups.

To quantify EdU+ cells *in vivo*, a stock of 50mg 5-ethynyl-2-deoxyuridine (EdU) (Alfagene, A10044) was diluted in 5mL of PBS to make a working solution (10mg/mL). EdU solution was injected intraperitoneally (200mg/kg) 4 hours before the

18

504 animals were sacrificed. Retinas were isolated and fixed as previously described, and

505 the EdU-positive cells were detected according to the user manual of the Click-iT EdU

506 Alexa Fluor 555 Imaging Kit (Invitrogen , C10338).

507 To affect glucose metabolism during shunt formation, PFKFB3 inhibitor (3PO; 50 µg/g)

508 (525330, Merck Life Sciences) or 2-deoxy-glucose (2-DG; 500 µg/g) (25972, Merck

509 Life Sciences) were injected IP at Day 0, Day 1, and Day 2 and pups were collected at

510 D3. For both treatments, PBS was injected in control pups. mTOR pathway was

511 inhibited using everolimus (13,5 µg/g) (73124, Stemcell) in peanut oil at Day 0, Day 1

512 and Day 2 to study shunt formation. Ethanol (vehicle) diluted in corn oil was injected to

513 control pups.

514 Vascular perfusion was assessed by injecting 10 µl of DyLight-649 conjugated

515 Lycopersicon Esculentum (Tomato) lectin (DL-1178-1, Vector Laboratories)

516 intracardially (1mg/mL) in anesthetise pups at let circulate for a minimum of 5 min time

517 before mouse sacrifice and eye collection.

518

Hyperoxia chamber protocol

520 P8 pups and their nursing mothers were housed in a Biospherix A-Chamber

521 (Biospherix) equipped with a ProOx 110 oxygen controller (Biospherix). In the

522 chamber, the animals were exposed to 75% oxygen level from P8 until they return to

523 normal room air conditions at P11, also termed as Day 0. Pups were sacrificed at the

524 time points. Eyes were collected and fixed with 2% PFA (15710, Electron Microscopy

525 Sciences) in PBS for 4 hours at 4°C.

526

Immunofluorescence on mouse retinas

528 Retinas were dissected in PBS and stained according to previously established

529 protocols[79,80]. Briefly, retinas were incubated on a rocking platform for 2 hours at room

530 temperature (RT) in Claudio's blocking buffer (CBB) consisting of 1% FBS (LTID

531 10500-064, Thermo Fisher), 3% BSA (MB04602, Nzytech), 0.5% Triton X100 (T8787,

532 Sigma Aldrich), 0.01% sodium deoxycholate (30970, Sigma Aldrich), 0.02% sodium

533 azide (S2002, Sigma Aldrich) in PBS, pH=7.4. Primary antibodies (see Table 1) were

534 incubated in 1:1 CBB/PBS overnight on a rocking platform at 4°C. Afterwards, retinas

535 were washed 3 times 30 minutes with PBS 0.1% triton X-100 (X100, Sigma Aldrich).

Secondary antibodies (see Table 1) were incubated in 1:1 CBB/PBS overnight on a rocking platform overnight in the dark at 4°C. Then retinas were washed 3 times 30 minutes with PBS 0.1% Tween and mounted on slides using Vectashield mounting medium (H-1000, VectorLabs).

Tile-scan spanning of retinas were acquired on either a Zeiss Cell Observer Spinning Disk confocal microscope equipped with Zen blue software or a 3i Marianas SDC spinning disk confocal microscope equipped with SlideBook 6.0.22 software. An EC plan-neofluar Ph1 10x NA 0.30 dry objective, a plan-apochromat Ph2 20x NA 0.80 dry objective or an LD C-apochromat Corr 40x NA 1.10 water objective or a Plan-Apochromat DIC 40x NA 1.40 oil objective were used for the acquisitions. For EC volume, high-resolution images were obtained using a confocal laser point-scanning microscope (Zeiss 980) equipped with the Zen software, using a plan-fluor apochromat 63x NA 1.40 oil objective.

Image analysis

Most of image analyses were performed with Fiji software[81]. Shunt occurrence was quantified manually as a ratio between the total AV shunt observed over the total AV sections quantified at a specific time point in a specific condition. Endothelial cell density was defined as the number of ERG+ or GFP+ (GNrep mouse strain) nuclei (quantified manually) over the CD31 corresponding surface (determined after thresholding based on fluorescence intensity). Endothelial proliferation was quantified manually as a ratio of the number of phospho-Histone H3/ERG or GFP double positive cells over the corresponding number of ERG or GFP+ cells. Diameters were quantified using the VasoMetrics Fiji tool[82] with a 10 μm step between crosslines. Mural cell coverage was quantified as a surface ratio of each marker with CD31 surface after thresholding based on fluorescence intensity. Polarity was defined manually based on the angle of nucleus-to-Golgi axis with estimated flow direction in three categories: with the flow (0-45°), random (45°-135°), and against the flow (135°-180°). Sprouts were quantified manually as the ration of branch point number to a specific vessel (AV shunt or vein) over the length of that vessel. Neovascularised area was defined as the CD31 surface (after thresholding based on fluorescence intensity) over the proximal surface delimited by the AV shunt, its corresponding artery and vein, and the optic nerve. Lectin

568 perfusion was quantified in two different ways. For neovascular area perfusion, it was

569 defined as the lectin signal surface (after thresholding based on fluorescence intensity)

570 over the proximal surface. For connection perfusion, it was quantified as a ration

571 between the number of branch point positive for lectin and the total number of branch

572 point considered.

573 Cell volume was analysed using Imaris software (Oxford Instruments). High-resolution

574 images of single mGFP+ endothelial cells were acquired using a 980 confocal

575 microscope equipped with a 63X NA 1.40 oil objective. The mGFP channel was

576 segmented using "surfaces" segmentation tool to create a solid volume (sup.video 1).

577 Unsegmented signal arising from the low GFP signal at the nucleus was manually

578 corrected using Fiji.

579

580 **Statistical analysis**

581 All statistical analyses were performed using R Studio (R version 1.4.1717, R

582 Foundation for Statistical Computing). Quantifications were done on independent

583 samples. Each data point corresponds to a shunt or a single cell, and the number of

584 animals per experiment, as well as the number of litters, are stated in the figure legend.

585 Statistical details of experiments are reported in the figures and their legends. No

586 inclusion, exclusion or randomization criteria were used and all analysed samples were

587 included. Comparisons between two experimental groups were analysed using Mann-

588 Whitney test. Multiple comparisons between more than two experimental groups were

589 assessed with Kruskal Wallis test and combined with Dunn post-hoc test using

590 Benjamini & Hochberg correction for p-value adjustment. Proportion comparisons were

591 analysed using Fisher exact t-test and combined with Fisher post-hoc test using

592 Benjamini & Hochberg correction for p-value adjustment in the case of multiple

593 comparisons. A result was considered significant when $p < 0.05$.

594

595

References

1.   Alaraj A, Shakur SF, Amin-Hanjani S, Mostafa H, Khan S, Aletich VA and Charbel FT. Changes in wall shear stress of cerebral arteriovenous malformation feeder arteries after embolization and surgery. *Stroke*. 2015;46:1216-20.

2.   Steiger HJ. Recent progress understanding pathophysiology and genesis of brain AVM-a narrative review. *Neurosurg Rev*. 2021;44:3165-3175.

3.   Couto JA, Huang AY, Konczyk DJ, Goss JA, Fishman SJ, Mulliken JB, Warman ML and Greene AK. Somatic MAP2K1 Mutations Are Associated with Extracranial Arteriovenous Malformation. *Am J Hum Genet*. 2017;100:546-554.

4.   Nikolaev SI, Vetiska S, Bonilla X, Boudreau E, Jauhiainen S, Rezai Jahromi B, Khyzha N, DiStefano PV, Suutarinen S, Kiehl TR, Mendes Pereira V, Herman AM, Krings T, Andrade-Barazarte H, Tung T, Valiante T, Zadeh G, Tymianski M, Rauramaa T, Yla-Herttuala S, Wythe JD, Antonarakis SE, Frosen J, Fish JE and Radovanovic I. Somatic Activating KRAS Mutations in Arteriovenous Malformations of the Brain. *N Engl J Med*. 2018;378:250-261.

5.   Dupuis-Girod S, Bailly S and Plauchu H. Hereditary hemorrhagic telangiectasia: from molecular biology to patient care. *J Thromb Haemost*. 2010;8:1447-56.

6.   Robert F, Desroches-Castan A, Bailly S, Dupuis-Girod S and Feige JJ. Future treatments for hereditary hemorrhagic telangiectasia. *Orphanet J Rare Dis*. 2020;15:4.

7.   Johnson DW, Berg JN, Baldwin MA, Gallione CJ, Marondel I, Yoon SJ, Stenzel TT, Speer M, Pericak-Vance MA, Diamond A, Guttmacher AE, Jackson CE, Attisano L, Kucherlapati R, Porteous ME and Marchuk DA. Mutations in the activin receptor-like kinase 1 gene in hereditary haemorrhagic telangiectasia type 2. *Nat Genet*. 1996;13:189-95.

8.   Lesca G, Burnichon N, Raux G, Tosi M, Pinson S, Marion MJ, Babin E, Gilbert-Dussardier B, Riviere S, Goizet C, Faivre L, Plauchu H, Frebourg T, Calender A, Giraud S and French Rendu-Osler N. Distribution of ENG and ACVRL1 (ALK1) mutations in French HHT patients. *Hum Mutat*. 2006;27:598.

9.   McAllister KA, Grogg KM, Johnson DW, Gallione CJ, Baldwin MA, Jackson CE, Helmbold EA, Markel DS, McKinnon WC, Murrell J and et al. Endoglin, a TGF-beta binding protein of endothelial cells, is the gene for hereditary haemorrhagic telangiectasia type 1. *Nat Genet*. 1994;8:345-51.

10.   Gallione CJ, Repetto GM, Legius E, Rustgi AK, Schelley SL, Tejpar S, Mitchell G, Drouin E, Westermann CJ and Marchuk DA. A combined syndrome of juvenile polyposis and hereditary haemorrhagic telangiectasia associated with mutations in MADH4 (SMAD4). *Lancet*. 2004;363:852-9.

11.   Gallione CJ, Richards JA, Letteboer TG, Rushlow D, Prigoda NL, Leedom TP, Ganguly A, Castells A, Ploos van Amstel JK, Westermann CJ, Pyeritz RE and Marchuk DA. SMAD4 mutations found in unselected HHT patients. *J Med Genet*. 2006;43:793-7.

12.   Hernandez F, Huether R, Carter L, Johnston T, Thompson J, Gossage JR, Chao E and Elliott AM. Mutations in RASA1 and GDF2 identified in patients with clinical features of hereditary hemorrhagic telangiectasia. *Hum Genome Var*. 2015;2:15040.

13.   Liu J, Yang J, Tang X, Li H, Shen Y, Gu W and Zhao S. Homozygous GDF2-Related Hereditary Hemorrhagic Telangiectasia in a Chinese Family. *Pediatrics*. 2020;146.

14.   Topiwala KK, Patel SD, Nouh AM and Alberts MJ. Novel GDF2 Gene Mutation Associated with Pulmonary Arteriovenous Malformation. *J Stroke Cerebrovasc Dis*. 2020;29:105301.

15.   Wooderchak-Donahue WL, McDonald J, O'Fallon B, Upton PD, Li W, Roman BL, Young S, Plant P, Fulop GT, Langa C, Morrell NW, Botella LM, Bernabeu C, Stevenson DA, Runo JR and Bayrak-Toydemir P. BMP9 mutations cause a vascular-anomaly syndrome with phenotypic overlap with hereditary hemorrhagic telangiectasia. *Am J Hum Genet*. 2013;93:530-7.

16.   Lee HW, Xu Y, He L, Choi W, Gonzalez D, Jin SW and Simons M. Role of Venous Endothelial Cells in Developmental and Pathologic Angiogenesis. *Circulation*. 2021;144:1308-1322.

17.   Park H, Furtado J, Poulet M, Chung M, Yun S, Lee S, Sessa WC, Franco CA, Schwartz MA and Eichmann A. Defective Flow-Migration Coupling Causes Arteriovenous Malformations in Hereditary Hemorrhagic Telangiectasia. *Circulation*. 2021;144:805-822.

18. Singh E, Redgrave RE, Phillips HM and Arthur HM. Arterial endoglin does not protect against arteriovenous malformations. *Angiogenesis*. 2020;23:559-566.

19. Baeyens N, Larrivee B, Ola R, Hayward-Piatkowskyi B, Dubrac A, Huang B, Ross TD, Coon BG, Min E, Tsarfati M, Tong H, Eichmann A and Schwartz MA. Defective fluid shear stress mechanotransduction mediates hereditary hemorrhagic telangiectasia. *J Cell Biol*. 2016;214:807-16.

20. Corti P, Young S, Chen CY, Patrick MJ, Rochon ER, Pekkan K and Roman BL. Interaction between alk1 and blood flow in the development of arteriovenous malformations. *Development*. 2011;138:1573-82.

21. Jin Y, Muhl L, Burmakin M, Wang Y, Duchez AC, Betsholtz C, Arthur HM and Jakobsson L. Endoglin prevents vascular malformation by regulating flow-induced cell migration and specification through VEGFR2 signalling. *Nat Cell Biol*. 2017;19:639-652.

22. Murphy PA, Kim TN, Lu G, Bollen AW, Schaffer CB and Wang RA. Notch4 normalization reduces blood vessel size in arteriovenous malformations. *Sci Transl Med*. 2012;4:117ra8.

23. Park SO, Lee YJ, Seki T, Hong KH, Fliess N, Jiang Z, Park A, Wu X, Kaartinen V, Roman BL and Oh SP. ALK5- and TGFBR2-independent role of ALK1 in the pathogenesis of hereditary hemorrhagic telangiectasia type 2. *Blood*. 2008;111:633-42.

24. Park SO, Wankhede M, Lee YJ, Choi EJ, Fliess N, Choe SW, Oh SH, Walter G, Raizada MK, Sorg BS and Oh SP. Real-time imaging of de novo arteriovenous malformation in a mouse model of hereditary hemorrhagic telangiectasia. *J Clin Invest*. 2009;119:3487-96.

25. Ola R, Dubrac A, Han J, Zhang F, Fang JS, Larrivee B, Lee M, Urarte AA, Kraehling JR, Genet G, Hirschi KK, Sessa WC, Canals FV, Graupera M, Yan M, Young LH, Oh PS and Eichmann A. PI3 kinase inhibition improves vascular malformations in mouse models of hereditary haemorrhagic telangiectasia. *Nat Commun*. 2016;7:13650.

26. Han C, Choe SW, Kim YH, Acharya AP, Keselowsky BG, Sorg BS, Lee YJ and Oh SP. VEGF neutralization can prevent and normalize arteriovenous malformations in an animal model for hereditary hemorrhagic telangiectasia 2. *Angiogenesis*. 2014;17:823-830.

27. Ruiz S, Zhao H, Chandakkar P, Papoin J, Choi H, Nomura-Kitabayashi A, Patel R, Gillen M, Diao L, Chatterjee PK, He M, Al-Abed Y, Wang P, Metz CN, Oh SP, Blanc L, Campagne F and Marambaud P. Correcting Smad1/5/8, mTOR, and VEGFR2 treats pathology in hereditary hemorrhagic telangiectasia models. *J Clin Invest*. 2020;130:942-957.

28. Fish JE, Flores Suarez CP, Boudreau E, Herman AM, Gutierrez MC, Gustafson D, DiStefano PV, Cui M, Chen Z, De Ruiz KB, Schexnayder TS, Ward CS, Radovanovic I and Wythe JD. Somatic Gain of KRAS Function in the Endothelium Is Sufficient to Cause Vascular Malformations That Require MEK but Not PI3K Signaling. *Circ Res*. 2020;127:727-743.

29. Crist AM, Lee AR, Patel NR, Westhoff DE and Meadows SM. Vascular deficiency of Smad4 causes arteriovenous malformations: a mouse model of Hereditary Hemorrhagic Telangiectasia. *Angiogenesis*. 2018;21:363-380.

30. Sugden WW, Meissner R, Aegerter-Wilmsen T, Tsaryk R, Leonard EV, Bussmann J, Hamm MJ, Herzog W, Jin Y, Jakobsson L, Denz C and Siekmann AF. Endoglin controls blood vessel diameter through endothelial cell shape changes in response to haemodynamic cues. *Nat Cell Biol*. 2017;19:653-665.

31. Rochon ER, Menon PG and Roman BL. Alk1 controls arterial endothelial cell migration in lumenized vessels. *Development*. 2016;143:2593-602.

32. Banerjee K, Lin Y, Gahn J, Gupta P, Graupera M, Dobreva G, Schwartz M and Ola R. Excessive fluid shear stress-mediated Klf4 leads to arteriovenous pathogenesis. *bioRxiv*. 2022:2022.07.04.498236.

33. Ricci B. Oxygen-induced retinopathy in the rat model. *Doc Ophthalmol*. 1990;74:171-7.

34. Scott A and Fruttiger M. Oxygen-induced retinopathy: a model for vascular pathology in the retina. *Eye (Lond)*. 2010;24:416-21.

35. Penn JS, Madan A, Caldwell RB, Bartoli M, Caldwell RW and Hartnett ME. Vascular endothelial growth factor in eye disease. *Prog Retin Eye Res*. 2008;27:331-71.

697   36.   Chang E, Nayak L and Jain MK. Kruppel-like factors in endothelial cell biology. *Curr Opin*
698   *Hematol*. 2017;24:224-229.
699   37.   Ola R, Kunzel SH, Zhang F, Genet G, Chakraborty R, Pibouin-Fragner L, Martin K, Sessa W,
700   Dubrac A and Eichmann A. SMAD4 Prevents Flow Induced Arteriovenous Malformations by Inhibiting
701   Casein Kinase 2. *Circulation*. 2018;138:2379-2394.
702   38.   Murphy PA, Kim TN, Huang L, Nielsen CM, Lawton MT, Adams RH, Schaffer CB and Wang RA.
703   Constitutively active Notch4 receptor elicits brain arteriovenous malformations through enlargement
704   of capillary-like vessels. *Proc Natl Acad Sci U S A*. 2014;111:18007-12.
705   39.   Verweij J and Pinedo HM. Mitomycin C: mechanism of action, usefulness and limitations.
706   *Anticancer Drugs*. 1990;1:5-13.
707   40.   Barbacena P, Ouarne M, Haigh JJ, Vasconcelos FF, Pezzarossa A and Franco CA. GNrep mouse:
708   A reporter mouse for front-rear cell polarity. *Genesis*. 2019;57:e23299.
709   41.   Figueiredo AM, Barbacena P, Russo A, Vaccaro S, Ramalho D, Pena A, Lima AP, Ferreira RR,
710   Fidalgo MA, El-Marjou F, Carvalho Y, Vasconcelos FF, Lennon-Dumenil AM, Vignjevic DM and Franco
711   CA. Endothelial cell invasion is controlled by dactylopodia. *Proc Natl Acad Sci U S A*. 2021;118.
712   42.   Franco CA, Blanc J, Parlakian A, Blanco R, Aspalter IM, Kazakova N, Diguet N, Mylonas E, Gao-
713   Li J, Vaahtokari A, Penard-Lacronique V, Fruttiger M, Rosewell I, Mericskay M, Gerhardt H and Li Z. SRF
714   selectively controls tip cell invasive behavior in angiogenesis. *Development*. 2013;140:2321-33.
715   43.   Franco CA, Mericskay M, Parlakian A, Gary-Bobo G, Gao-Li J, Paulin D, Gustafsson E and Li Z.
716   Serum response factor is required for sprouting angiogenesis and vascular integrity. *Dev Cell*.
717   2008;15:448-461.
718   44.   Weinl C, Riehle H, Park D, Stritt C, Beck S, Huber G, Wolburg H, Olson EN, Seeliger MW, Adams
719   RH and Nordheim A. Endothelial SRF/MRTF ablation causes vascular disease phenotypes in murine
720   retinae. *J Clin Invest*. 2013;123:2193-206.
721   45.   Muzumdar MD, Tasic B, Miyamichi K, Li L and Luo L. A global double-fluorescent Cre reporter
722   mouse. *Genesis*. 2007;45:593-605.
723   46.   Sorensen I, Adams RH and Gossler A. DLL1-mediated Notch activation regulates endothelial
724   identity in mouse fetal arteries. *Blood*. 2009;113:5680-8.
725   47.   Aspalter IM, Gordon E, Dubrac A, Ragab A, Narloch J, Vizan P, Geudens I, Collins RT, Franco CA,
726   Abrahams CL, Thurston G, Fruttiger M, Rosewell I, Eichmann A and Gerhardt H. Alk1 and Alk5 inhibition
727   by Nrp1 controls vascular sprouting downstream of Notch. *Nat Commun*. 2015;6:7264.
728   48.   Hikita T, Mirzapourshafiyi F, Barbacena P, Riddell M, Pasha A, Li M, Kawamura T, Brandes RP,
729   Hirose T, Ohno S, Gerhardt H, Matsuda M, Franco CA and Nakayama M. PAR-3 controls endothelial
730   planar polarity and vascular inflammation under laminar flow. *EMBO reports*. 2018;19:e45253.
731   49.   Rohlenova K, Veys K, Miranda-Santos I, De Bock K and Carmeliet P. Endothelial Cell Metabolism
732   in Health and Disease. *Trends Cell Biol*. 2018;28:224-236.
733   50.   Pajak B, Siwiak E, Soltyka M, Priebe A, Zielinski R, Fokt I, Ziemniak M, Jaskiewicz A, Borowski R,
734   Domoradzki T and Priebe W. 2-Deoxy-d-Glucose and Its Analogs: From Diagnostic to Therapeutic
735   Agents. *Int J Mol Sci*. 2019;21.
736   51.   De Bock K, Georgiadou M, Schoors S, Kuchnio A, Wong BW, Cantelmo AR, Quaegebeur A,
737   Ghesquiere B, Cauwenberghs S, Eelen G, Phng LK, Betz I, Tembuyser B, Brepoels K, Welti J, Geudens I,
738   Segura I, Cruys B, Bifari F, Decimo I, Blanco R, Wyns S, Vangindertael J, Rocha S, Collins RT, Munck S,
739   Daelemans D, Imamura H, Devlieger R, Rider M, Van Veldhoven PP, Schuit F, Bartrons R, Hofkens J,
740   Fraisl P, Telang S, Deberardinis RJ, Schoonjans L, Vinckier S, Chesney J, Gerhardt H, Dewerchin M and
741   Carmeliet P. Role of PFKFB3-driven glycolysis in vessel sprouting. *Cell*. 2013;154:651-63.
742   52.   Saxton RA and Sabatini DM. mTOR Signaling in Growth, Metabolism, and Disease. *Cell*.
743   2017;168:960-976.
744   53.   Tual-Chalot S, Mahmoud M, Allinson KR, Redgrave RE, Zhai Z, Oh SP, Fruttiger M and Arthur
745   HM. Endothelial depletion of Acvrl1 in mice leads to arteriovenous malformations associated with
746   reduced endoglin expression. *PLoS One*. 2014;9:e98646.
747   54.   Barbacena P, Dominguez-Cejudo M, Fonseca CG, Gomez-Gonzalez M, Faure LM, Zarkada G,
748   Pena A, Pezzarossa A, Ramalho D, Giarratano Y, Ouarne M, Barata D, Fortunato IC, Misikova LH,

749 Mauldin I, Carvalho Y, Trepat X, Roca-Cusachs P, Eichmann A, Bernabeu MO and Franco CA.
750 Competition for endothelial cell polarity drives vascular morphogenesis in the mouse retina. *Dev Cell*.
751 2022;57:2321-2333 e9.

752 55.   Franco CA, Jones ML, Bernabeu MO, Geudens I, Mathivet T, Rosa A, Lopes FM, Lima AP, Ragab
753 A, Collins RT, Phng LK, Coveney PV and Gerhardt H. Dynamic endothelial cell rearrangements drive
754 developmental vessel regression. *PLoS Biol*. 2015;13:e1002125.

755 56.   Franco CA, Jones ML, Bernabeu MO, Vion A-C, Barbacena P, Fan J, Mathivet T, Fonseca CG,
756 Ragab A, Yamaguchi TP, Coveney PV, Lang RA and Gerhardt H. Non-canonical Wnt signalling modulates
757 the endothelial shear stress flow sensor in vascular remodelling. *eLife*. 2016;5:e07727.

758 57.   Ouarne M, Pena A and Franco CA. From remodeling to quiescence: The transformation of the
759 vascular network. *Cells Dev*. 2021;168:203735.

760 58.   Nielsen CM, Zhang X, Raygor K, Wang S, Bollen AW and Wang RA. Endothelial Rbpj deletion
761 normalizes Notch4-induced brain arteriovenous malformation in mice. *J Exp Med*. 2023;220.

762 59.   Cadart C, Venkova L, Recho P, Lagomarsino MC and Piel M. The physics of cell-size regulation
763 across timescales. *Nature Physics*. 2019;15:993-1004.

764 60.   Sachs F and Sivaselvan MV. Cell volume control in three dimensions: Water movement without
765 solute movement. *J Gen Physiol*. 2015;145:373-80.

766 61.   Schmelzle T and Hall MN. TOR, a central controller of cell growth. *Cell*. 2000;103:253-62.

767 62.   Dang CV. MYC, metabolism, cell growth, and tumorigenesis. *Cold Spring Harbor perspectives*
768 *in medicine*. 2013;3.

769 63.   Schuhmacher M, Staege MS, Pajic A, Polack A, Weidle UH, Bornkamm GW, Eick D and
770 Kohlhuber F. Control of cell growth by c-Myc in the absence of cell division. *Curr Biol*. 1999;9:1255-8.

771 64.   Dong J, Feldmann G, Huang J, Wu S, Zhang N, Comerford SA, Gayyed MF, Anders RA, Maitra A
772 and Pan D. Elucidation of a universal size-control mechanism in Drosophila and mammals. *Cell*.
773 2007;130:1120-33.

774 65.   Mugahid D, Kalocsay M, Liu X, Gruver JS, Peshkin L and Kirschner MW. YAP regulates cell size
775 and growth dynamics via non-cell autonomous mediators. *Elife*. 2020;9.

776 66.   Yu FX, Zhao B and Guan KL. Hippo Pathway in Organ Size Control, Tissue Homeostasis, and
777 Cancer. *Cell*. 2015;163:811-28.

778 67.   Guo M, Pegoraro AF, Mao A, Zhou EH, Arany PR, Han Y, Burnette DT, Jensen MH, Kasza KE,
779 Moore JR, Mackintosh FC, Fredberg JJ, Mooney DJ, Lippincott-Schwartz J and Weitz DA. Cell volume
780 change through water efflux impacts cell stiffness and stem cell fate. *Proc Natl Acad Sci U S A*.
781 2017;114:E8618-E8627.

782 68.   Perez Gonzalez N, Tao J, Rochman ND, Vig D, Chiu E, Wirtz D and Sun SX. Cell tension and
783 mechanical regulation of cell volume. *Mol Biol Cell*. 2018;29:0.

784 69.   Zhu W, Saw D, Weiss M, Sun Z, Wei M, Shaligram S, Wang S and Su H. Induction of Brain
785 Arteriovenous Malformation Through CRISPR/Cas9-Mediated Somatic Alk1 Gene Mutations in Adult
786 Mice. *Transl Stroke Res*. 2019;10:557-565.

787 70.   Longden TA, Zhao G, Hariharan A and Lederer WJ. Pericytes and the Control of Blood Flow in
788 Brain and Heart. *Annu Rev Physiol*. 2023;85:137-164.

789 71.   Li F, Lan Y, Wang Y, Wang J, Yang G, Meng F, Han H, Meng A, Wang Y and Yang X. Endothelial
790 Smad4 maintains cerebrovascular integrity by activating N-cadherin through cooperation with Notch.
791 *Dev Cell*. 2011;20:291-302.

792 72.   Nadeem T, Bogue W, Bigit B and Cuervo H. Deficiency of Notch signaling in pericytes results in
793 arteriovenous malformations. *JCI Insight*. 2020;5.

794 73.   Pan P, Shaligram SS, Do Prado LB, He L and Su H. The role of mural cells in hemorrhage of brain
795 arteriovenous malformation. *Brain Hemorrhages*. 2021;2:49-56.

796 74.   Boon LM, Dekeuleneer V, Coulie J, Marot L, Bataille A-C, Hammer F, Clapuyt P, Jeanjean A,
797 Dompmartin A and Vikkula M. Case report study of thalidomide therapy in 18 patients with severe
798 arteriovenous malformations. *Nature Cardiovascular Research*. 2022;1:562-567.

799 75.   Lebrin F, Srun S, Raymond K, Martin S, van den Brink S, Freitas C, Breant C, Mathivet T, Larrivee
800 B, Thomas JL, Arthur HM, Westermann CJ, Disch F, Mager JJ, Snijder RJ, Eichmann A and Mummery CL.

Thalidomide stimulates vessel maturation and reduces epistaxis in individuals with hereditary hemorrhagic telangiectasia. *Nat Med*. 2010;16:420-8.

76.   Krndija D, El Marjou F, Guirao B, Richon S, Leroy O, Bellaiche Y, Hannezo E and Matic Vignjevic D. Active cell migration is critical for steady-state epithelial turnover in the gut. *Science*. 2019;365:705-710.

77.   Parlakian A, Tuil D, Hamard G, Tavernier G, Hentzen D, Concordet JP, Paulin D, Li Z and Daegelen D. Targeted inactivation of serum response factor in the developing heart results in myocardial defects and embryonic lethality. *Mol Cell Biol*. 2004;24:5281-9.

78.   Claxton S, Kostourou V, Jadeja S, Chambon P, Hodivala-Dilke K and Fruttiger M. Efficient, inducible Cre-recombinase activation in vascular endothelium. *Genesis*. 2008;46:74-80.

79.   Bernabeu MO, Jones ML, Nash RW, Pezzarossa A, Coveney PV, Gerhardt H and Franco CA. PolNet: A Tool to Quantify Network-Level Cell Polarity and Blood Flow in Vascular Remodeling. *Biophys J*. 2018;114:2052-2058.

80.   Carvalho JR, Fortunato IC, Fonseca CG, Pezzarossa A, Barbacena P, Dominguez-Cejudo MA, Vasconcelos FF, Santos NC, Carvalho FA and Franco CA. Non-canonical Wnt signaling regulates junctional mechanocoupling during angiogenic collective cell migration. *Elife*. 2019;8.

81.   Schindelin J, Arganda-Carreras I, Frise E, Kaynig V, Longair M, Pietzsch T, Preibisch S, Rueden C, Saalfeld S, Schmid B, Tinevez J-Y, White DJ, Hartenstein V, Eliceiri K, Tomancak P and Cardona A. Fiji: an open-source platform for biological-image analysis. *Nature Methods*. 2012;9:676-682.

82.   McDowell KP, Berthiaume AA, Tieu T, Hartmann DA and Shih AY. VasoMetrics: unbiased spatiotemporal analysis of microvascular diameter in multi-photon imaging applications. *Quant Imaging Med Surg*. 2021;11:969-982.

Acknowledgements

Author Contributions

Conceptualization: MO, AP, DR, SPO, CAF

Methodology: MO, AP, DR, NVC, TC, SPO, CAF

Experimentation and data acquisition: MO, AP, DR, NVC, TC, AF, MPS, YC, LHM, CAF

Data analysis: MO, AP, DR, NVC, TC, CAF

Project administration: CAF

Writing – original draft: MO, CAF

Writing – review & editing: MO, AP, DR, NVC, SPO, CAF

Competing Interests

The authors declare that they have no competing interests.

Figure Legends

Figure 1 – OIR protocol forms transient AV shunts independent of genetic alterations.

A, Top panel: schematic of the experimental protocol. Bottom panel: Representative images of mouse retinas stained for CD31 (grey) on Day 1, Day 3, Day 5, and Day 7. Black arrows: AV shunt; A: artery; V: vein. Scale bar: 200 μm. **B,** Quantification of AV shunt prevalence between Day 0 and Day 8. Day 0: 51 AV sections (8 pups); Day 1: 44 AV sections (8 pups); Day 2: 56 AV sections (8 pups); Day 3: 66 AV sections (8 pups); Day 4: 55 AV sections (7 pups); Day 5: 50 AV sections (7 pups); Day 5: 50 AV sections (7 pups); Day 6: 41 AV sections (6 pups); Day 7: 30 AV sections (4 pups); Day 8: 4 AV sections (1 pup). **C,** Representative image of an AV shunt at Day 3 highlighting its perfusion status (lectin, cyan) and co-stained for ECs (CD31, magenta). Arrowhead: AV shunt; A: artery; V: vein. Scale bar: 100 μm. **D,** Representative image of smooth muscle coverage (αSMA, cyan) of an AV shunt at Day 4 co-stained for ECs (CD31, magenta). Arrowhead: AV shunt; A: artery; V: vein. Scale bar: 100 μm. **E,** Representative image of an AV shunt at Day 3 stained for ECs (CD31, grey), pSmad1 (cyan) and KLF4 (magenta). Arrowhead: AV shunt; A: artery; V: vein. Scale bar: 100 μm.

Figure 2 – Fine time-course analysis of AV shunt formation.

A, Representative images of mouse retinas at 28h and 36h stained for CD31 (grey). Black arrow: AV shunt; A: artery; V: vein. Scale bar: 200 μm. **B,** Quantification of total AV shunt prevalence every 4h between 24h and 48h. 24h: 44 AV sections (8 pups); 28h: 31 AV sections (7 pups); 32h: 29 AV sections (5 pups); 36h: 34 AV sections (5 pups); 40h: 23 AV sections (3 pups); 44h: 23 AV sections (3 pups); 48h: 56 AV sections (8 pups). P-values from Fisher exact t-test and Fisher post-hoc test using Benjamini & Hochberg correction for multiple comparisons. **C,** Representative images of arterial (top) and venous (bottom) second-order vessels (A: artery a: arteriole, V: vein, v: venule) at 0h, 24h, and 32h of AV shunt protocol exposed mouse retinas stained for CD31 (grey). Scale bar: 50 μm. **D,** Quantification of arteriole (top), first (bottom) and second (middle) venule normalized diameter (% of mean diameter at Day 0) between 0h and 40h. Each dot represents a second-order vessel from: Day 0 (3 pups); 24h (3 pups); 28h (2 pups); 32h (3 pups); 36h (3 pups); and 40h (2 pups). P-values from Kruskal Wallis test and Dunn post-hoc test using Benjamini & Hochberg correction for multiple comparisons.

877 **Figure 3 – EC proliferation and migration have minor contributions to AV shunt**
878 **formation.**

879 **A,** Representative image of proliferating (pHH3, green, white arrows) EC nuclei (ERG, red)
880 within the vasculature (CD31, blue) of a Day 2 OIR mouse retina. The dotted line delineates
881 forming AV shunt. Scale bar: 50 μm. **B,** Quantification of percentage of proliferative ECs
882 (pHH3/ERG ratio) in capillaries, arteries and veins between Day 0 and Day 2. Each dot
883 represents a vessel from Day 0 (4 pups); Day 1 (5 pups); and Day 2 (14 pups) retinas. P-
884 values from Kruskal Wallis test and Dunn post-hoc test using Benjamini & Hochberg correction
885 for multiple comparisons. **C,** Top panel: schematic of mitomycin C treatment. Black arrow: time
886 of vehicle or mitomycin C injection; purple arrow: time of collection. Bottom panel:
887 representative images of retinas at Day 3 treated with PBS or mitomycin C stained for ECs
888 (CD31, magenta) and proliferative cells (pHH3, cyan). White arrows: AV shunts; A: artery; V:
889 vein. Scale bar: 200 μm. **D,** Quantification of AV shunt prevalence at Day 3 in PBS (33 AV
890 sections, 5 pups) and mitomycin C (46 AV sections, 7 pups) treated retinas. P-value from
891 Mann-Whitney test. **E,** Quantification of AV shunt mean diameter at Day 3 in PBS (21 AV
892 sections, 3 pups) and mitomycin C (14 AV sections, 2 pups) treated retinas. P-value from
893 Mann-Whitney test. **F,** Top panel: schematic of the experimental protocol using Arpc4/Srf
894 mouse strains. Black arrow: tamoxifen injection; purple arrow: time of collection.
895 Representative images of Arpc4-WT and Arpc4-iECKO retinas on Day 3 stained for ECs
896 (CD31, grey). Black arrows: AV shunts; A: artery; V: vein. Scale bar: 200 μm. **G,** Quantification
897 of AV shunt prevalence at Day 3 in Arpc4-WT (91 AV sections, 7 pups) and Arpc4-iECKO (57
898 AV sections, 5 pups) retinas. P-value from Mann-Whitney test. **H,** Quantification of AV shunt
899 mean diameter at Day 3 in Arpc4-WT (7 pups) and Arpc4-iECKO (5 pups) retinas. Each dot
900 represents an AV shunt. P-value from Mann-Whitney test. **I,** Quantification of AV shunt
901 prevalence at Day 3 in Srf-WT (85 AV sections, 12 pups) and Srf-iECKO (45 AV sections, 5
902 pups) retinas. P-value from Mann-Whitney test.

903

904 **Figure 4 – EC volume and venule diameter increases precede AV shunt development.**

905 **A,** Representative images of EC nuclei (ERG, red) distribution within artery, vein and capillary
906 at Day 0 and Day 1 (CD31, blue). Scale bar: 50 μm. **B,** Quantification of EC density in arteries,
907 veins, arterial capillaries and venous capillaries at Day 0 and Day 1. Each dot represents a
908 vessel on Day 0 (4 pups) and Day 1 (5 pups). P-value from Mann-Whitney test. **C,** Top panel:
909 schematic of experimental protocol for mosaic expression of mGFP in ECs. Black arrow:
910 tamoxifen injection; purple arrows: time of collection. Bottom panel: representative images of

911   single ECs (mGFP, grey) in the artery, arterial capillary, venous capillary, and vein from mouse

912   retinas at Day 0 and Day 1. Scale bar: 10 μm. **D,** Quantification of EC volume in single cells in

913   arteries, arterial capillaries, venous capillaries, and veins from mouse retinas at Day 0 and Day

914   1. Each dot represents an EC from Day 0 (3 pups) and Day 1 (3 pups). P-value from Mann-

915   Whitney test.

916

917   **Figure 5 – mTOR inhibition prevents EC volume increases and AV shunt formation.**

918   **A,** Top panel: schematic of AV shunt study protocol with everolimus treatment. Black arrows:

919   times of vehicle or everolimus injections; purple arrow: time of collection. Bottom panel:

920   representative images of single ECs (mGFP, grey) of retinas at Day 3 treated with vehicle or

921   everolimus. Scale bar: 10 μm. **B,** Quantification of EC volume in venous cells (veins and

922   venous capillaries) at Day 0, Day 1 and Day 3 mouse retinas treated with vehicle or everolimus.

923   Each dot represents one EC from Day 0 (3 pups), Day 1 (3 pups) and Day 3 (3 pups). P-value

924   from Krustal-Wallis test with Dunn's correction for multiple comparisons. **C,** Representative

925   images of retinas at Day 3 treated with vehicle or everolimus stained for ECs (CD31, grey).

926   Black arrows: AV shunts; A: artery; V: vein. Scale bar: 200 μm. **D,** Quantification of AV shunt

927   prevalence at Day 3 in vehicle (43 AV sections, 4 pups) and everolimus (54 AV sections, 5

928   pups) treated retinas. P-value from Mann-Whitney test**. E,** Quantification of AV shunt mean

929   diameter at Day 3 in vehicle (4 pups) and everolimus (5 pups) treated retinas. Each dot

930   represents an AV shunt. P-value from Mann-Whitney test.

931

932   **Figure 6 – Alk1 signaling controls EC volume cell-autonomously.**

933   **A,** Model describing AV shunt formation in OIR protocol. **B,** Quantification of arteriole and

934   venule diameter in Alk1-WT and Alk1-iECKO retinas 24h post tamoxifen injection. Each dot

935   represents a second-order vessel. P-value from Mann-Whitney test. **C,** Representative images

936   of ECs from a venous capillary EC (GFP, grey) of Alk1.iECHET-mTmG and Alk1-iECKO-

937   mTmG 24h post-tamoxifen injection. Scale bar: 10 μm. **D,** Quantification of EC volume in

938   arterial (arteries and arterial capillaries) and venous (vein and venous capillaries) vessels from

939   Alk1.iECHET-mTmG and Alk1-iECKO-mTmG 24h post-tamoxifen injection. Each dot

940   represents one EC from Alk1.iECHET-mTmG (2 pups) and Alk1-iECKO-mTmG (2 pups). P-

941   value from Mann-Whitney test.

942

Figure 7 – AV shunt regression correlates with perfusion of the neo-capillaries.

A, Representative images of mouse retinas stained for CD31 (grey) at Day 2, Day 3, Day 5, and Day 6. A: artery; V: vein. Scale bar: 500 μm. **B,** Quantification of neovascular capillary density between Day 2 and Day 6. Each dot represents an AV shunt proximal region from Day 2 (4 pups); Day 3 (3 pups); Day 4 (3 pups); Day 5 (4 pups); and Day 6 (2 pups). P-values from Kruskal-Wallis test and Dunn post-hoc test using Benjamini & Hochberg correction for multiple comparisons. **C,** Representative images of Day 5 mouse retinas perfused with lectin (red) and co-stained for ECs (CD31, green). A: artery; V: vein. Scale bar: 250 μm. **D,** Quantification of perfused neovascular capillary connections to AV shunt (top) and associated vein (bottom) between Day 2 and Day 6. Each dot represents an AV shunt or a vein from Day 2 (6 retinas); Day 3 (4 retinas); Day 4 (1 retina); Day 5 (5 retinas); and Day 6 (3 retinas). P-values from Kruskal-Wallis test with Dunn's correction for multiple comparisons. **E,** Quantification of AV shunt diameter on the first 50 μm connected to the corresponding artery (left) or vein (right) between Day 2 and Day 6 mouse retinas. Each dot represents an AV shunt from Day 2 (4 pups); Day 3 (3 pups); Day 4 (3 pups); Day 5 (4 pups); and Day 6 (2 pups). P-values from Kruskal-Wallis test and Dunn post-hoc test using Benjamini & Hochberg correction for multiple comparisons.

Figure 8 – Inhibition of neo-vascular capillaries prevents AV shunt regression.

A, Representative images of Arpc4-WT (top) and Arpc4-iECKO (bottom) retinas at Day 7 stained for vascular network (CD31, grey). Black arrows: AV shunts; A: artery; V: vein. Scale bar: 200 μm. **B,** Quantification of AV shunt prevalence at Day 7 in Arpc4-WT (29 AV sections) and Arpc4-iECKO (16 AV sections) retinas. P-value from Mann-Whitney test. **C,** Representative images of Srf-WT (top) and Srf-iECKO (bottom) retinas at Day 9 stained for vascular network (CD31, grey). Black arrows: AV shunts; A: artery; V: vein. Scale bar: 200 μm. **D,** Quantification of AV shunt prevalence at Day 9 in Srf-WT (86 AV sections) and Srf-iECKO (63 AV sections,) retinas. P-value from Mann-Whitney test. **E,** Quantification of venous (vein and venous capillaries) EC volume at Day 0, Day 1, Day 3, and Day 7 and of non-OIR mouse retinas corresponding to time points Day 0 (P11) and Day 7 (P18). Each dot represents one EC from Day 0 (3 pups,); Day 1 (3 pups); Day 3 (3 pups); Day 7 (2 pups); non-OIR Day 0 (2 pups); and non-OIR Day 7 (2 pups). P-values from Kruskal-Wallis test with Dunn's correction for multiple comparisons. **F,** Model describing AV shunt regression in OIR protocol.

Supplementary Figure 1 – Characterization of OIR-induced AV shunts.

A, Representative overview images of Day 3 mouse retinas stained for CD31 (grey). Red arrows: AV shunt; A: artery; V: vein. Scale bar: 500 μm. **B,** Quantification distance from optic nerve to capillaries (Day 0 and Day 1, left) or AV shunt (Days 2 to 6, right) on arteries or veins. Each dot represents an AV section from Day 0 and Day 1 (8 pups); and Days 2 to 6 (16 pups). P-values (ns) from Mann-Whitney test. **C,** Quantification of AV shunt mean diameterretinas exposed between Day 2 and Day 6. Each dot represents an AV shunt from Day 2 (4 pups); Day 3 (3 pups); Day 4 (3 pups); Day 5 (4 pups); and Day 6 (2 pups). P-values from Kruskal Wallis test and Dunn post-hoc test using Benjamini & Hochberg correction for multiple comparisons. **D,** Representative image of the vascular network stained for ECs (CD31, blue) and mural cells (αSMA, red; NG2, green) from a Day 4 mouse retina. Scale bar: 100 μm. **E,** Representative image of the vascular network stained for ECs (CD31, blue) mural cell coverage (desmin, red) from a Day 4 mouse retina. Scale bar: 100 μm.

Supplementary Figure 2 – Asymmetric increased vessel diameter occurs prior to OIR-induced AV shunts.

A, Representative images of mouse retinas stained for EC apical membrane (ICAM2, grey) at Day 0 and Day 1. A: artery; V: vein; a: arteriole; v: venule. Scale bar: 200 μm. **B,** Quantification of vessel diameter of arteries (left) and veins (right) from mouse retinas collected between Day 0 and 40h after returning to normoxia. Each dot represents a vessel from Day 0 (4 pups); 24h (4 pups); 28h (2 pups); 32h (4 pups); 36h (3 pups); and 40h (2 pups). P-value from Krustal-Wallis test with Dunn's correction for multiple comparisons.

Supplementary Figure 3 – OIR-induced AV shunts form independently of EC proliferation.

A, Representative images of Day 2 mouse retinas treated with PBS or MitoC stained for EC nuclei (ERG, red), proliferative cells (EdU, green) and EC membrane (CD31, blue). Arrowhead: AV shunt; A: artery; V: vein. Scale bar: 200 μm. **B,** Quantification of proliferative ECs (EdU/ERG ratio) in AV shunts at Day 2. Each dot represents a specific vessel bed from different retinas. P-values from Mann-Whitney test. **C,** Quantification of EC density in veins,

1007 capillaries and AV shunts from Day 3 retinas treated with PBS (4 pups) and mitomycin C (5

1008 pups). Each dot represents one vessel. P-values from Mann-Whitney test.

1009

Supplementary Figure 4 – Neither EC polarity nor EC migration is significantly associated with AV shunt development

1012 **A,** Representative image of a Day 1 GNrep mouse retina stained for ICAM2 (blue). EC nuclei

1013 are labelled by nGFP (green) and EC Golgi apparatuses are labelled by mCherry (red). A:

1014 artery; V: vein. Scale bar: 100 μm. Magnifications of an artery (top) and a vein (bottom).

1015 Red/blue arrows: blood flow direction in artery and vein, respectively; dotted white lines: vessel

1016 outline based on ICAM2 staining. **B,** Quantification of EC polarization pattern in arteries (top)

1017 and veins (bottom) between Day 0 and Day 3 retinas (3 pups for all conditions) and in non-

1018 OIR retinas (5 pups). P-values from Fisher exact t-test and Fisher post-hoc test using

1019 Benjamini & Hochberg correction for multiple comparisons. **C,** Representative image of a Day

1020 2 GNrep mouse retina stained for ICAM2 (blue). EC nuclei are labelled by nGFP (green) and

1021 EC Golgi apparatuses are labelled by mCherry (red). A: artery; V: vein. Scale bar: 100 μm.

1022 Highlights of AV shunt regions. Purple arrows blood flow direction; dotted white lines: vessel

1023 outline based on ICAM2 staining. **D,** Quantification of EC polarization proportions in AV shunt

1024 at Day 2 and Day 3 (3 pups). P-value from Fisher exact t-test and Fisher post-hoc test using

1025 Benjamini & Hochberg correction for multiple comparisons. **E,** Quantification of vein to

1026 neovascular capillary connections per μm in Day 3 Arpc4-WT (7 pups) and Arpc4-iECKO (5

1027 pups) mouse retinas. Each dot represents a vein. P-value from Mann-Whitney test. **F,**

1028 Quantification of vein to neovascular capillary connections per μm in Day 3 Srf-WT (8 pups)

1029 and Srf-iECKO (5 pups) mouse retinas. Each dot represents a vein. P-value from Mann-

1030 Whitney test. **G,** Representative images of Day 3 Srf-WT (top) and Srf-iECKO (bottom) retinas

1031 stained for ECs (CD31, grey). Black arrows: AV shunts; A: artery; V: vein. Scale bar: 100 μm.

1032 **H,** Quantification of AV shunt mean diameter in Day 3 in Srf-WT (6 pups) and Srf-iECKO (3

1033 pups) retinas. Each dot represents an AV shunt. P-value from Mann-Whitney test.

1034

Supplementary Figure 5 – A decrease in EC density precedes AV shunt formation.

1036 **A,** Representative images of Day 0 (top panel) and Day 1 (bottom panel) retinas stained for

1037 EC nuclei (ERG, red/grey) and EC membrane (CD31, blue) highlighting a decrease in EC

1038 density. Scale bar: 100 μm. Magnifications of arterial, venous and capillary regions.

1039

Supplementary Figure 6 – Inhibition of glycolysis does not alter EC volumes nor AV shunt formation.

A, Quantification of normalized EC volume (% mean EC volume at Day 0) in arteries, arterial capillaries, venous capillaries, and veins from Day 0 and Day 1. Each dot represents one EC from Day 0 (3 pups) and Day 1 (3 pups). P-values from Mann-Whitney test. **B,** Quantification of normalized EC volume (% mean cell volume in non-OIR) in arteries, arterial capillaries, venous capillaries, and veins from non-OIR and Day 0 retinas. Each dot represents one EC from non-OIR (2 pups) and Day 0 (3 pups). P-values from Mann-Whitney test. **C,** Representative images of Day 3 retinas treated with PBS or 2-DG or 3PO stained for ECs (CD31, grey). Red arrows: AV shunts; A: artery; V: vein. Scale bar: 100 μm. **D,** Quantification of AV shunt prevalence at Day 3 retinas treated with PBS (24 AV sections, 2 pups), 2-DG (18 AV sections, 2 pups), and 3PO (22 AV sections, 2 pups). P-values (ns) from Kruskal Wallis test and Dunn post-hoc test. **E,** Quantification of AV shunt mean diameter at Day 3 in retinas treated with PBS (2 pups), 2-DG (2 pups), and 3-PO (2 pups). Each dot represents an AV shunt. P-values from Kruskal Wallis test and Dunn´s correction for multiple comparisons. **F,** Representative image of a P6 Alk1-iECKO-mTmG retina iECKO-mTmG 24h post-tamoxifen injection highlighting mosaic activation of mGFP (green) and co-stained for EC membrane (CD31, blue) Scale bar: 200 μm.

1058

Supplementary Figure 7 – AV shunt regression does not involve EC apoptosis but requires neo-angiogenesis.

A, Representative image of a Day 5 retina stained for EC membrane (CD31, blue), EC nuclei (ERG, red) and apoptotic cells (active cleaved caspase 3, green). White arrows: AV shunts; A: artery; V: vein; red arrow: apoptotic EC. Scale bar: 100 μm. **B,** Quantification neovascular capillary connections arising from AV shunts (left) or veins (right) per μm from mouse retinas collected between Day 2 and Day 6. Each dot represents an AV shunt or a vein from Day 2 (4 pups); Day 3 (3 pups); Day 4 (3 pups); Day 5 (5 pups); and Day 6 (2 pups). P-values from Kruskal Wallis test and Dunn post-hoc test using Benjamini & Hochberg correction for multiple comparisons. **C,** Quantification of perfused neovascular capillary area (% of the proximal area) between Day 2 and Day 6. Each dot represents a proximal region from Day 2 (6 retinas); Day 3 (4 retinas); Day 4 (1 retina); Day 5 (5 retinas); and Day 6 (3 retinas). **D,** Quantification of the avascular area in Day 7 mouse retinas from in Arpc4-WT (4 pups) and Arpc4-iECKO (4 pups).

1072   Each dot represents a proximal AV shunt region. P-value from Mann-Whitney test. **E,**

1073   Quantification of the avascular area in Day 9 mouse retinas from Srf-WT (9 pups) and Srf-

1074   iECKO (7 pups). Each dot represents a proximal AV shunt region. P-value from Mann-Whitney

1075   test.

1076

1077   **Supplementary Video 1 – Example of EC volume segmentation.**

1078   3D rotational movie showing an example of a segmented single EC (yellow) from of a D1 Cdh5-

1079   CreERT::R26-mTmG retina. Retinas were stained for EC membrane (CD31, red) and EC

1080   nuclei (ERG, blue), and endogenous membrabar GFP signal is shown (green).

Figure 1
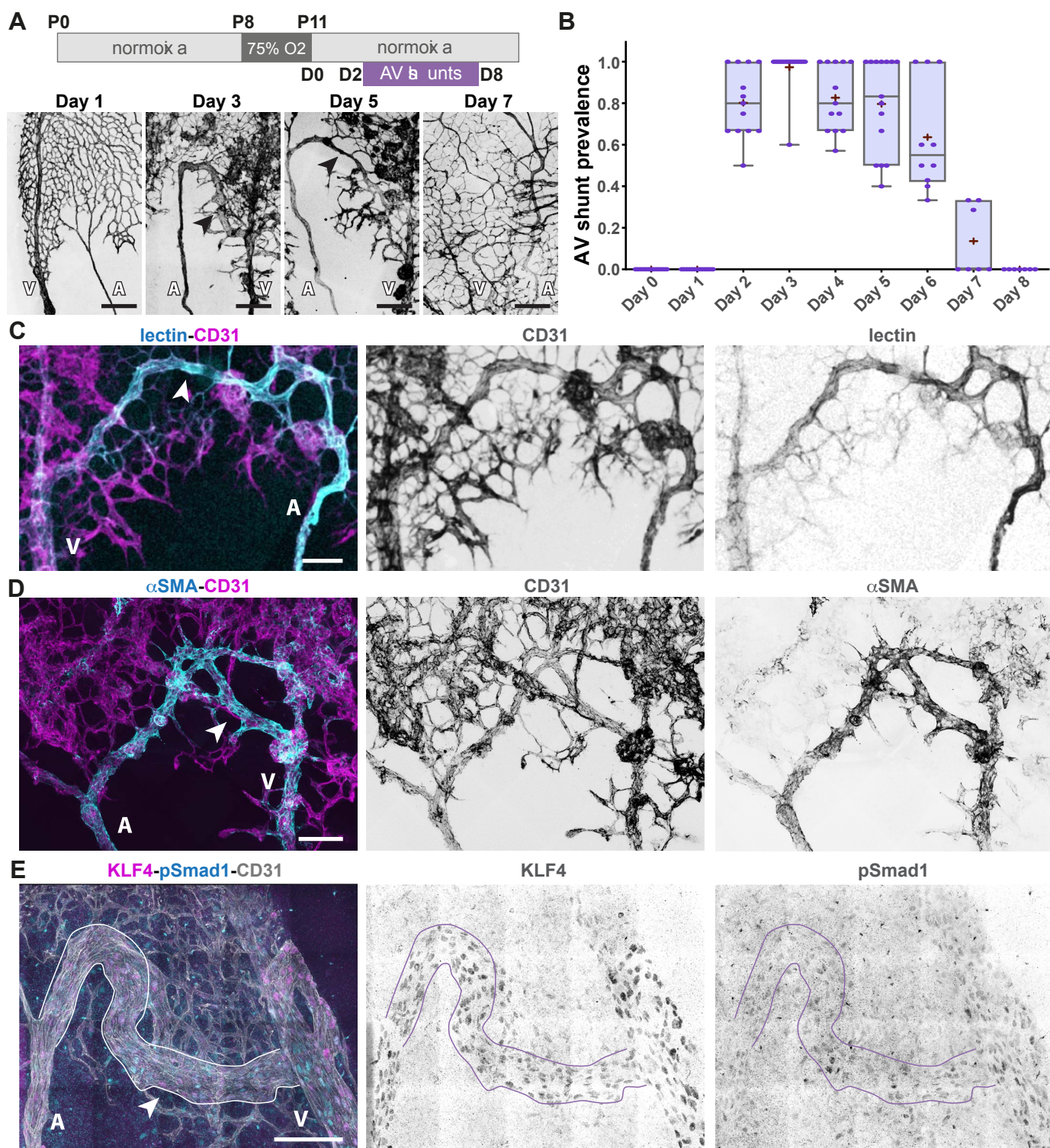
Figure 2
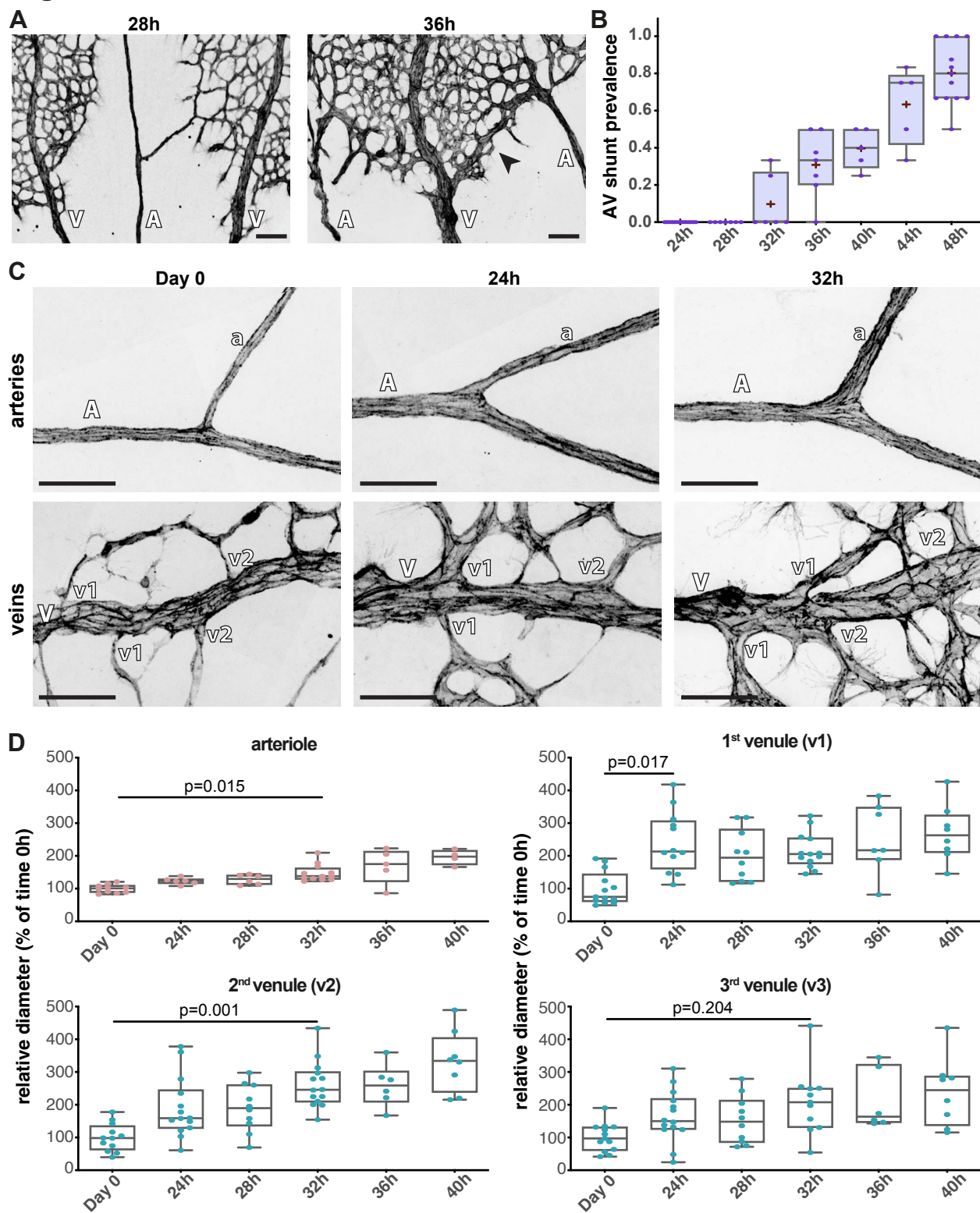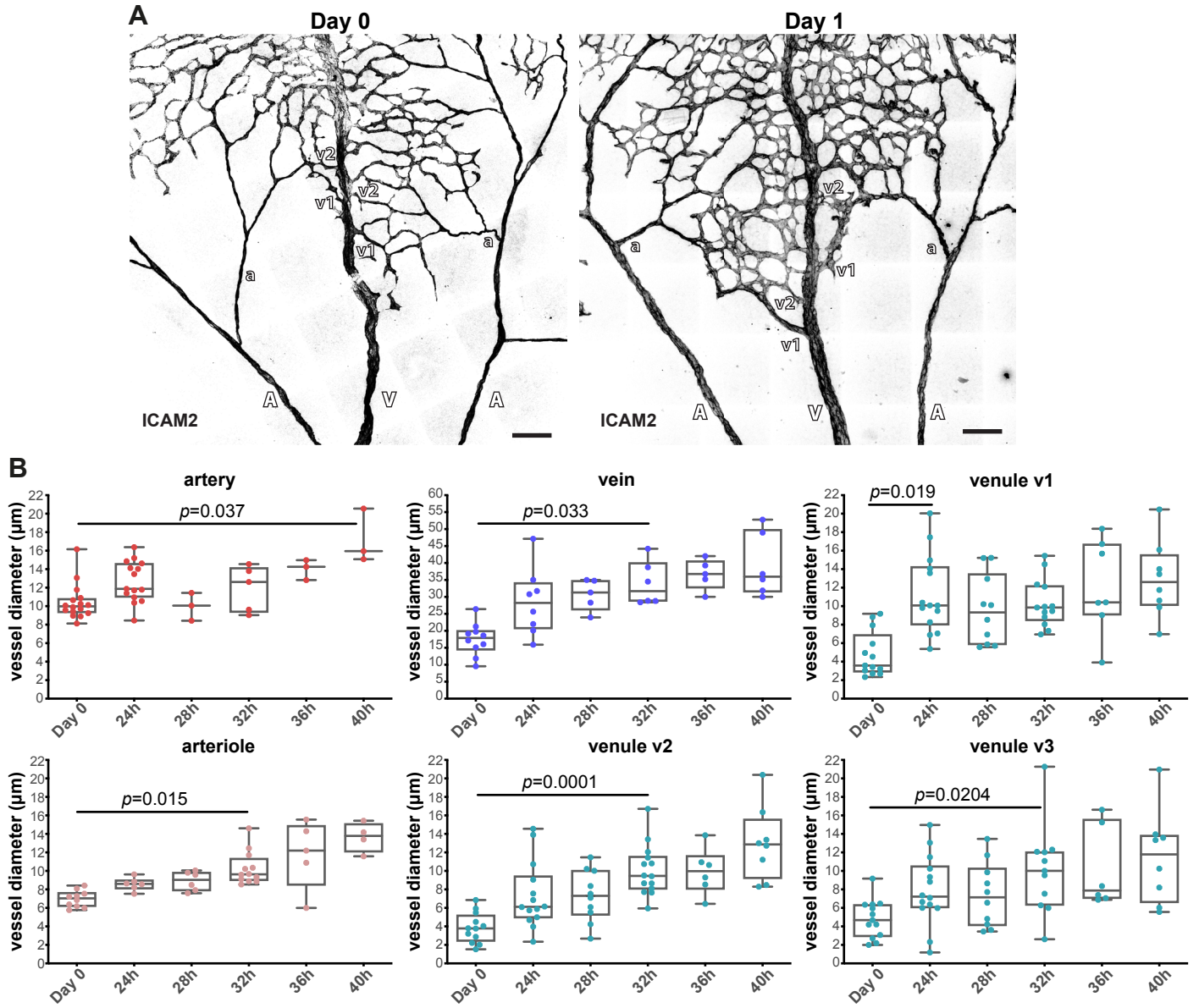
Figure 3
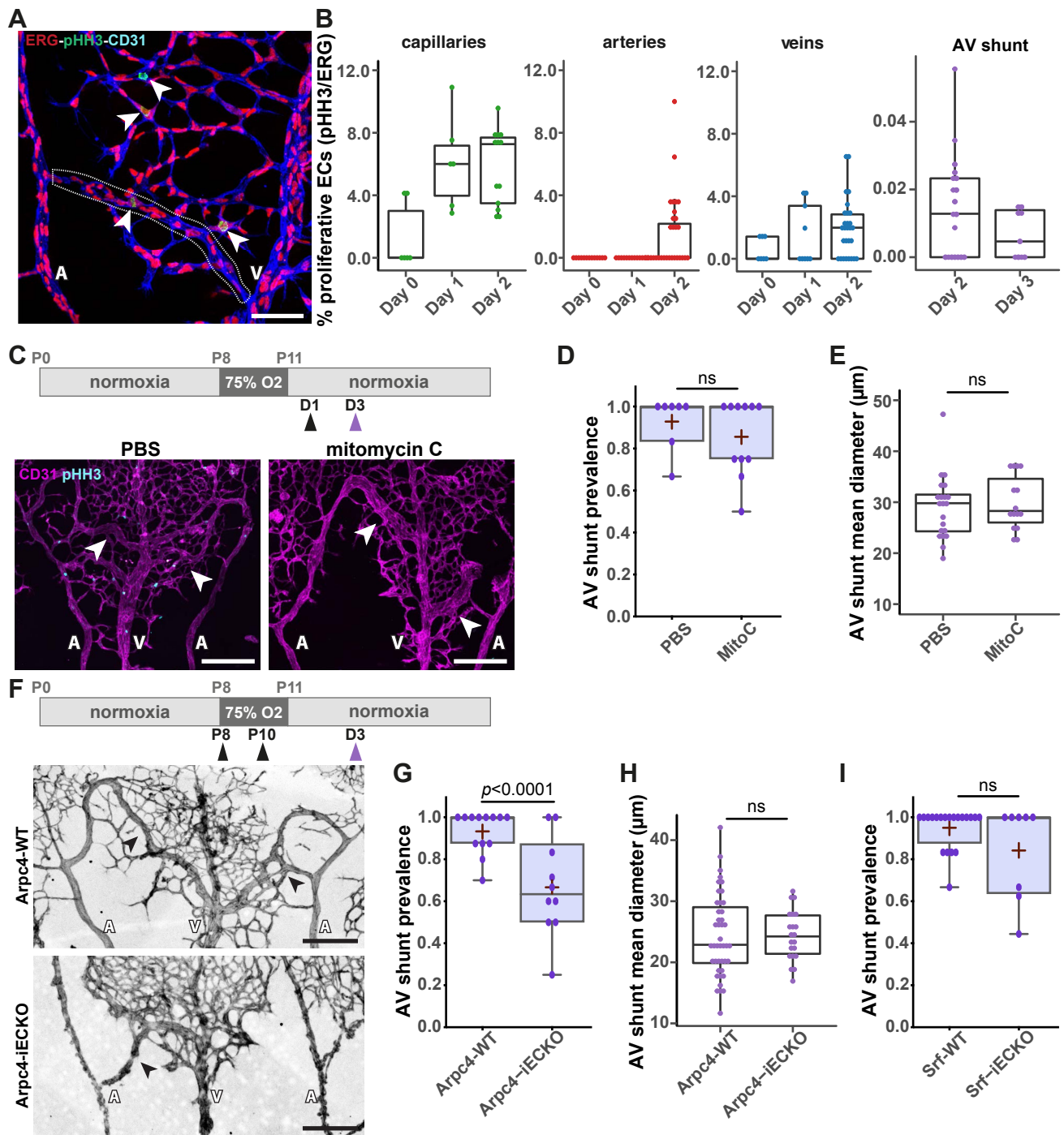
Figure 4
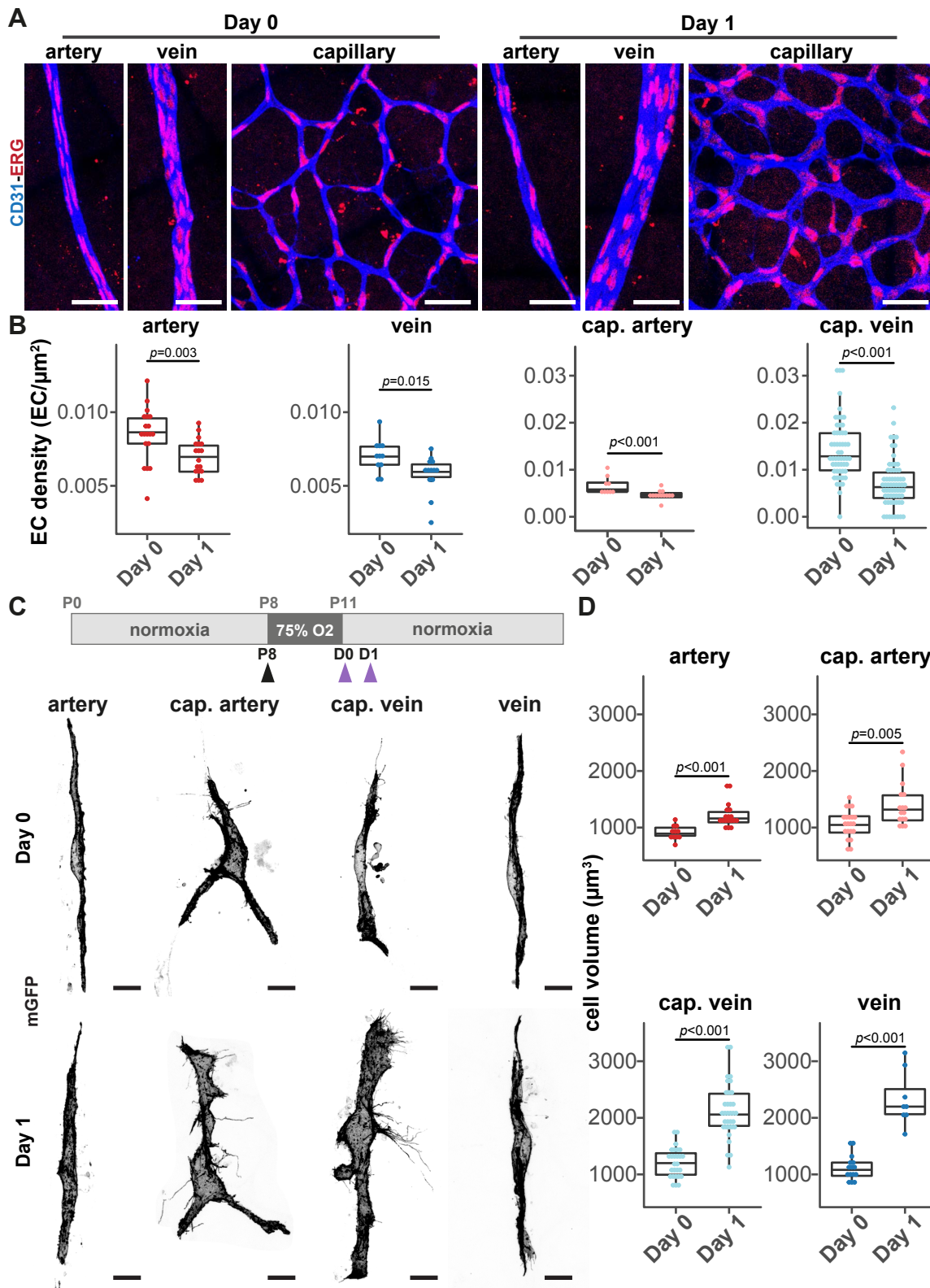
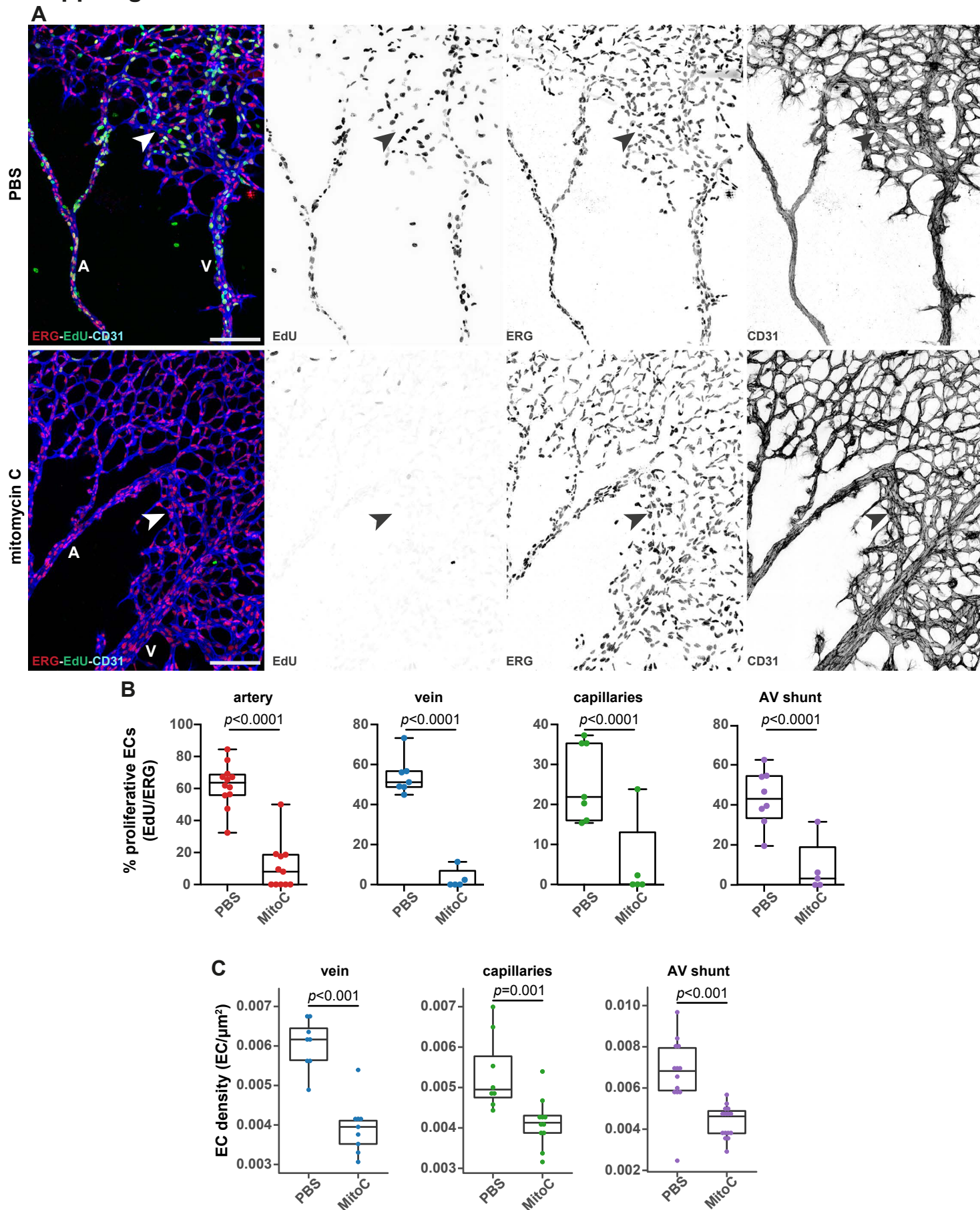# Figure 5
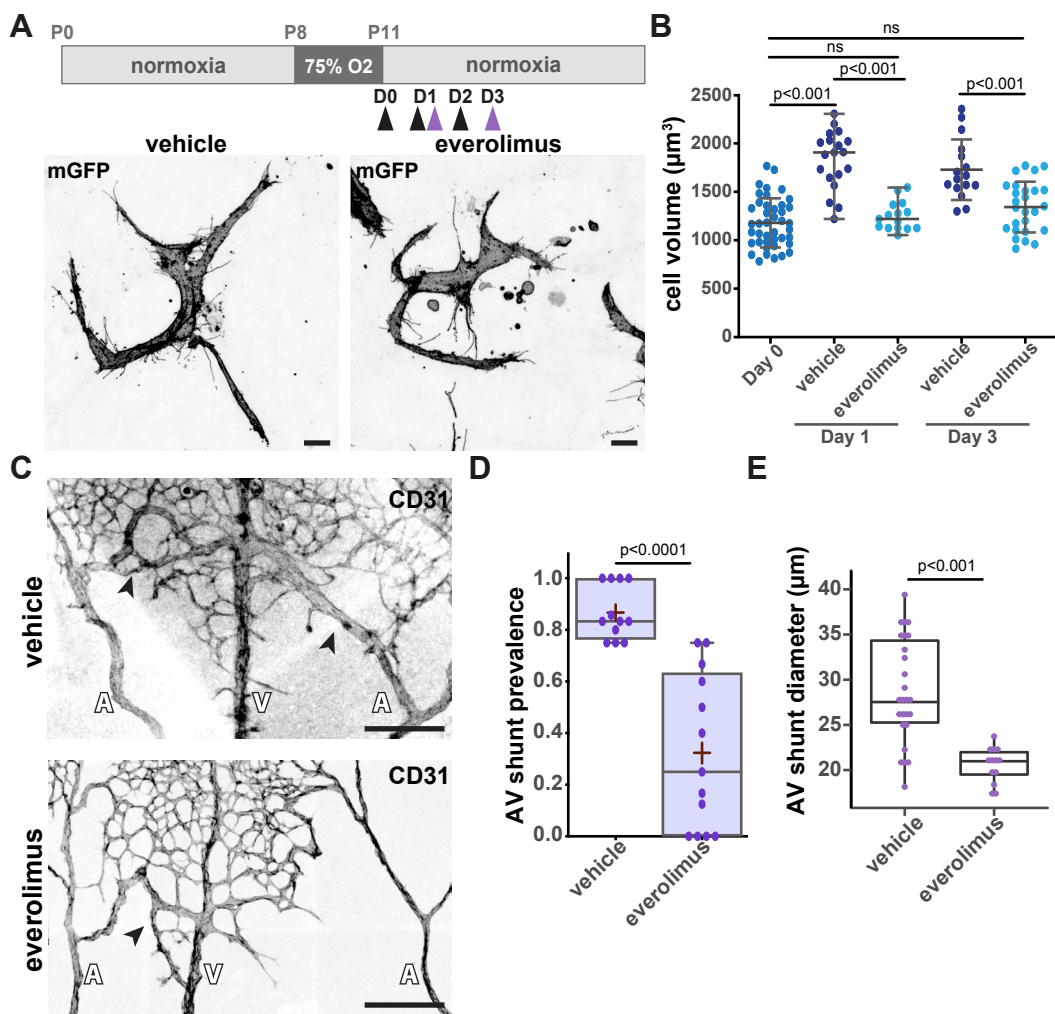
Figure 6
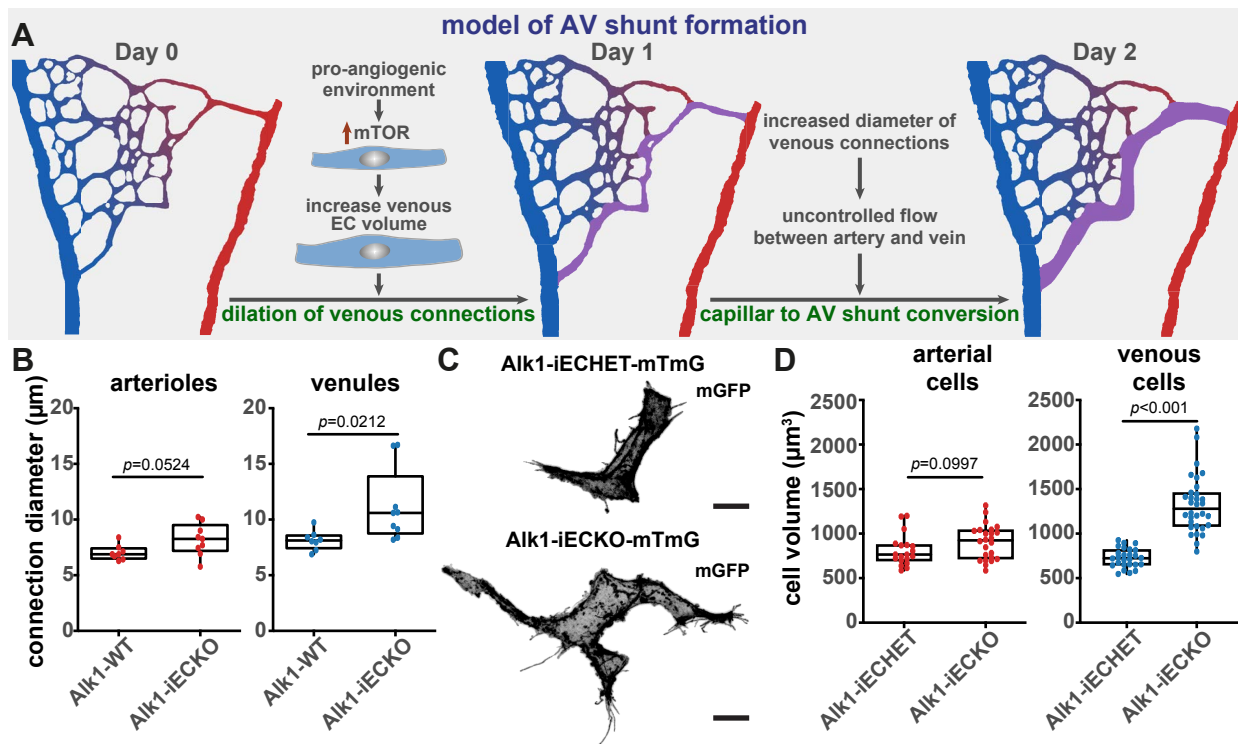
Figure 7
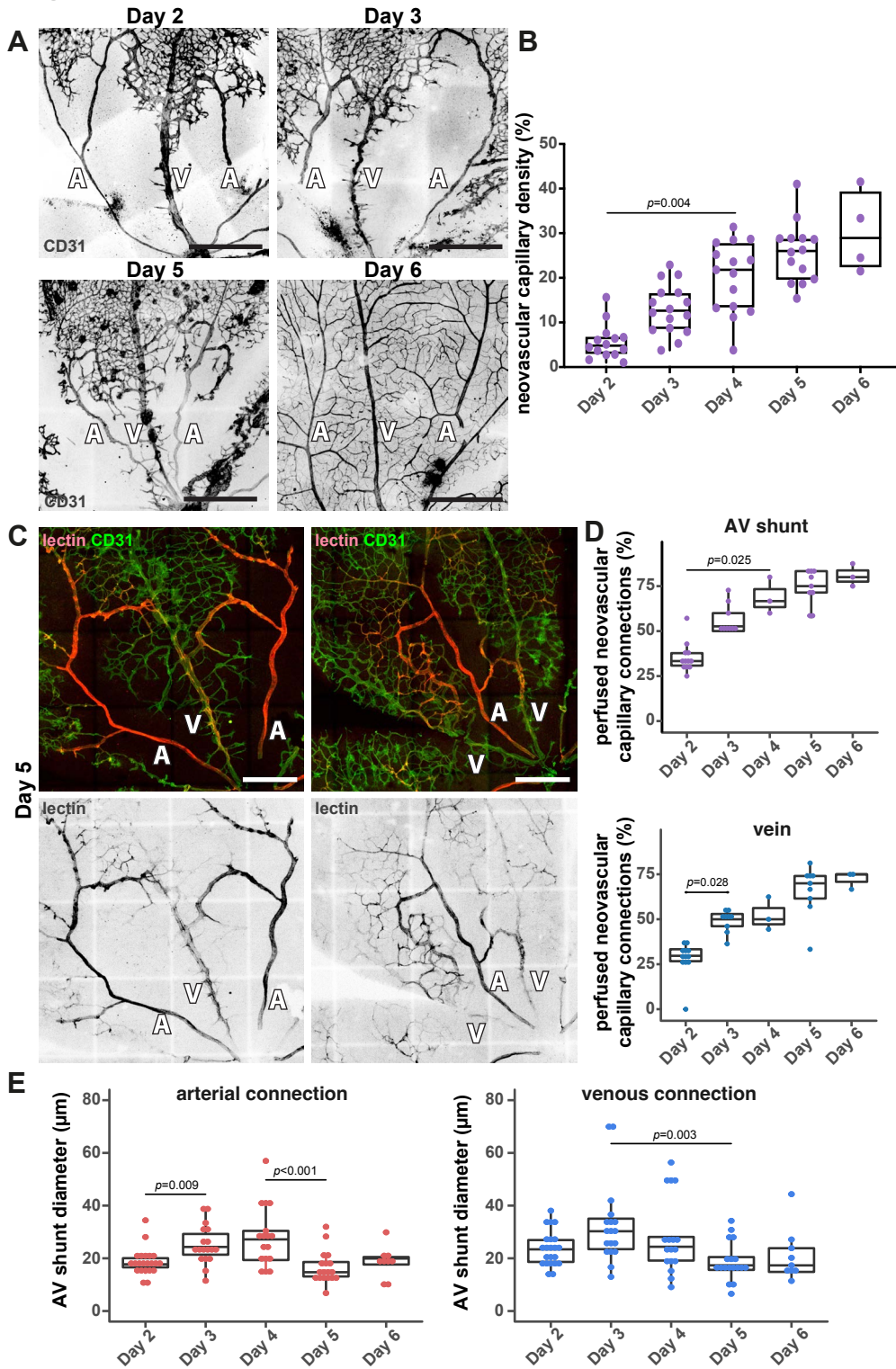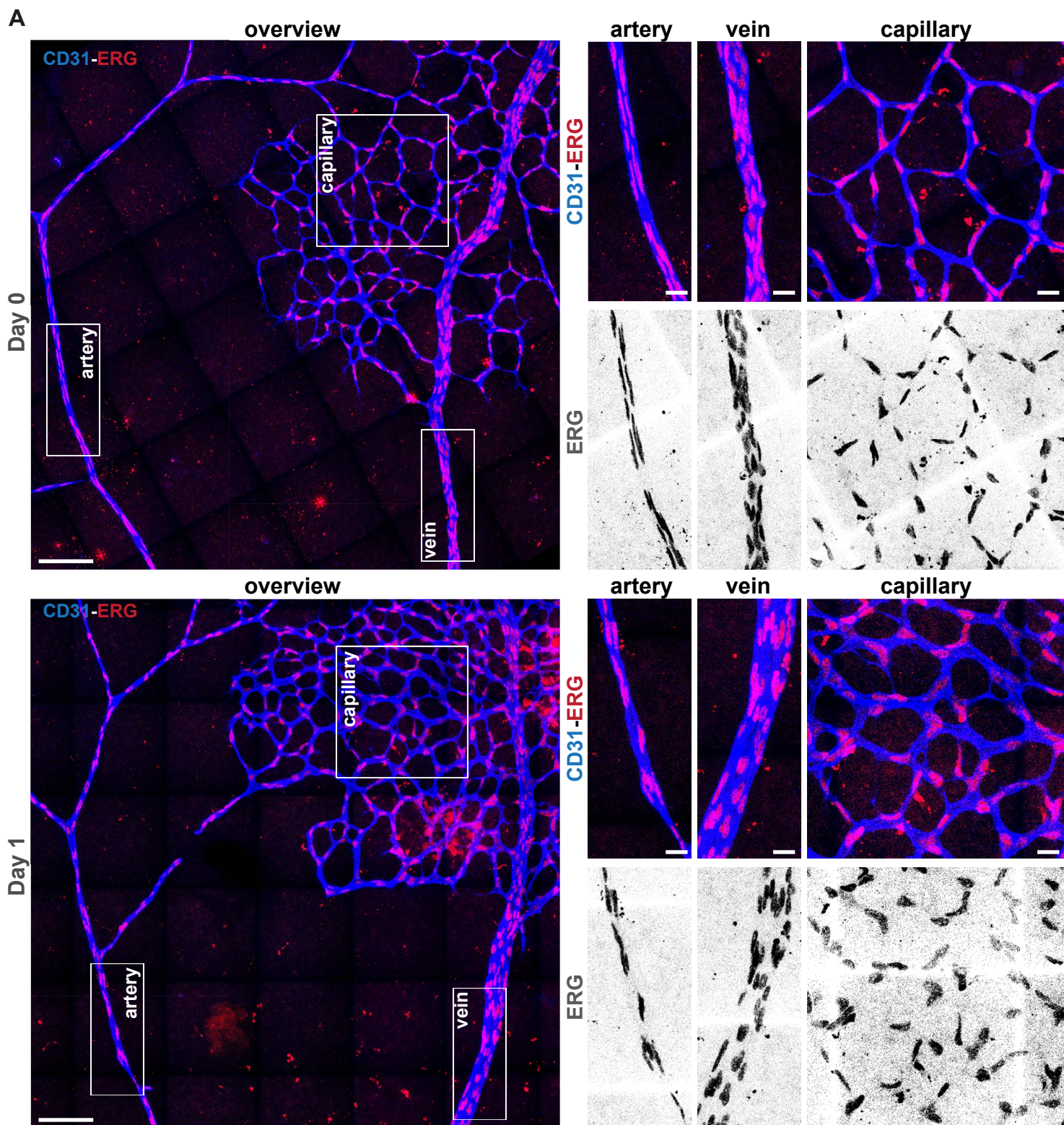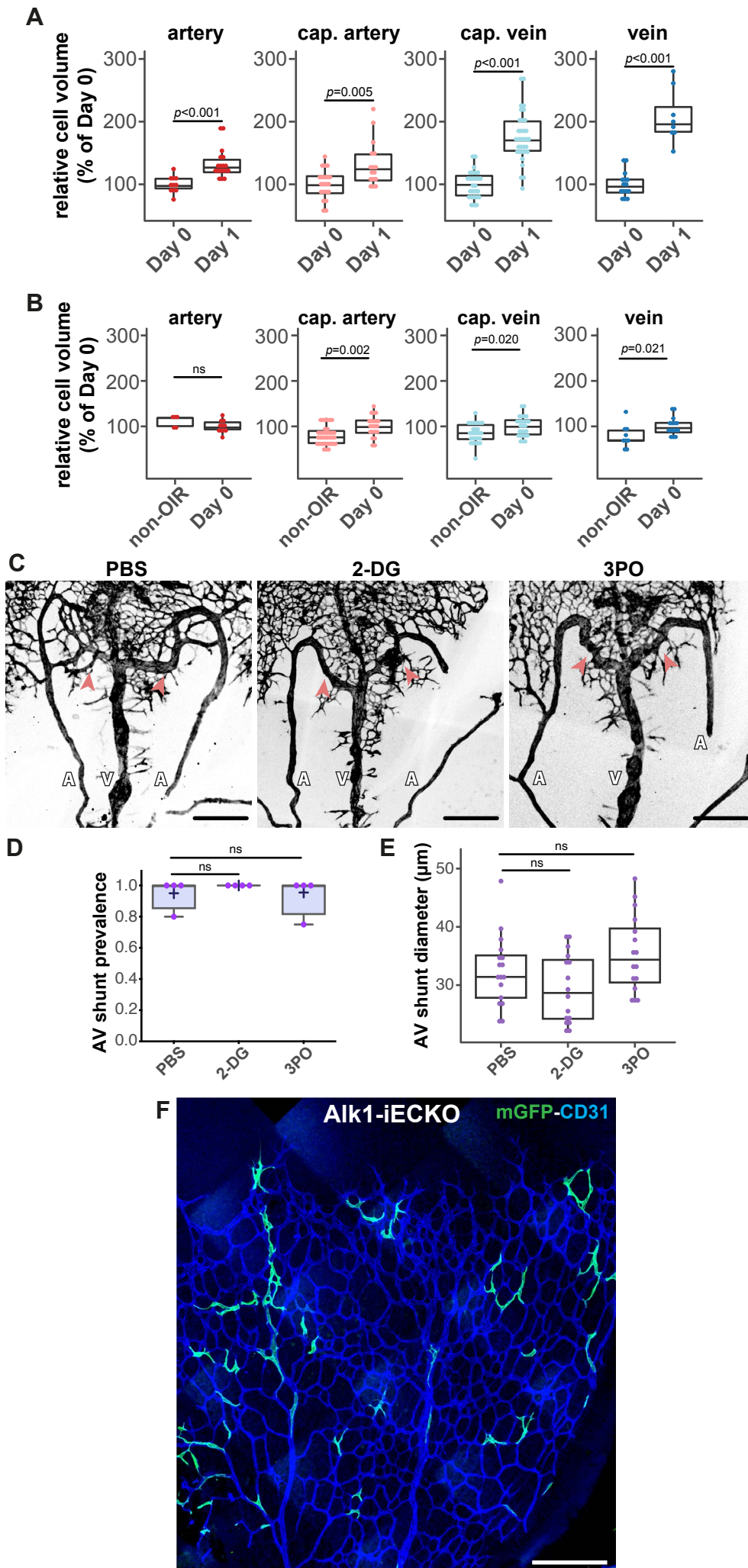
Figure 8
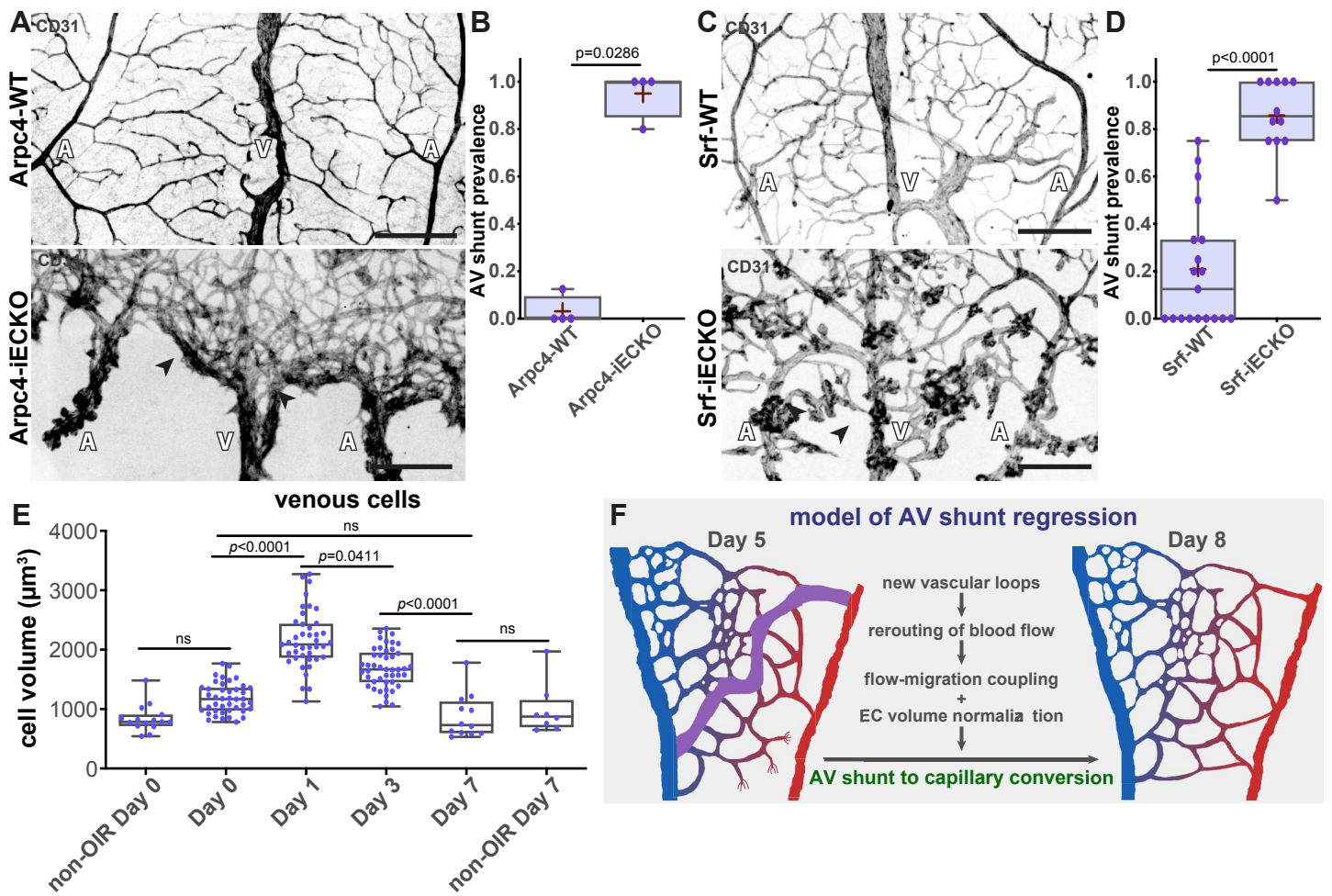
Supp. Figure 1
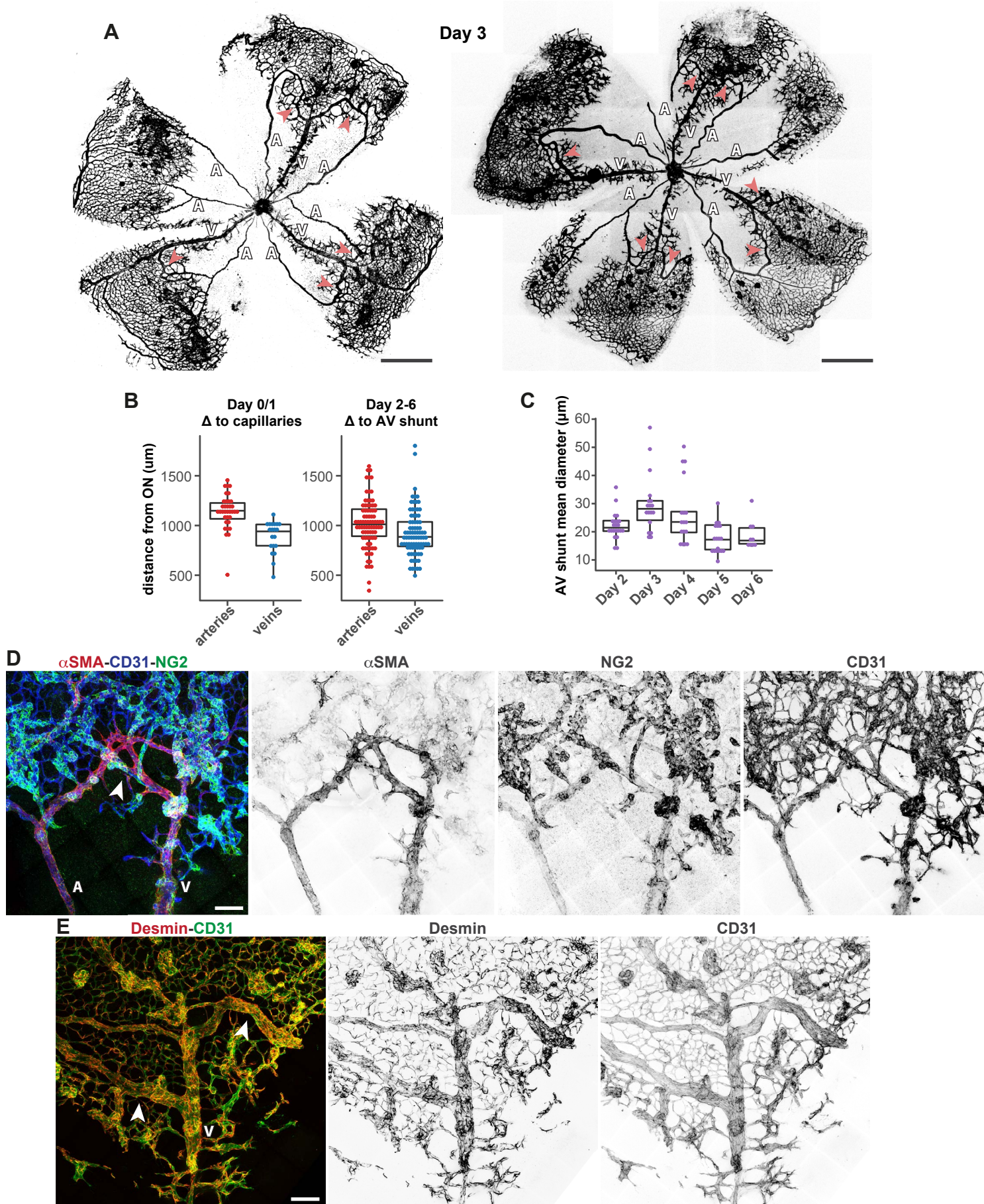
Supp. Figure 2

Supp. Figure 3

Supp. Figure 4
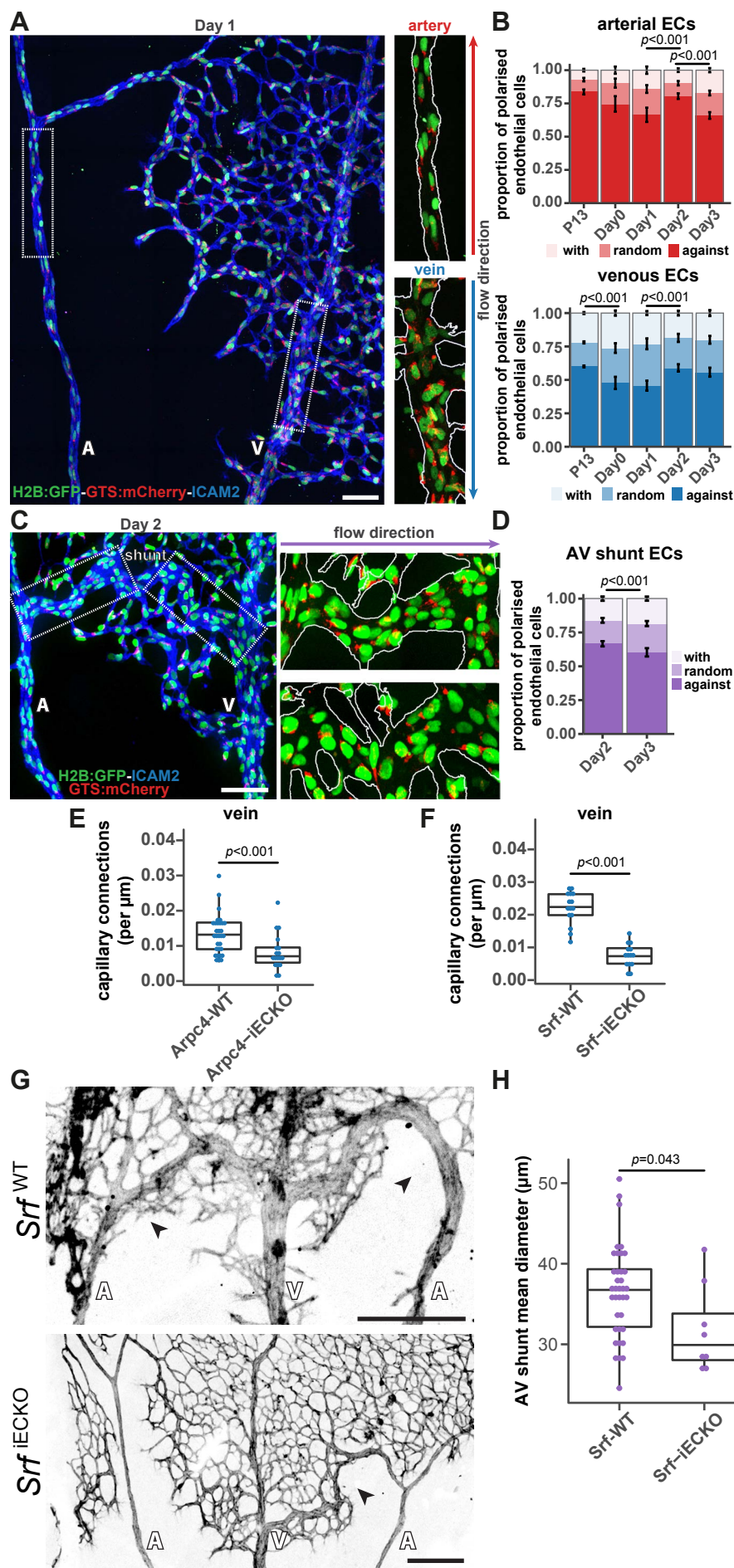
Supp. Figure 5

Supp. Figure 6

Supp. Figure 7
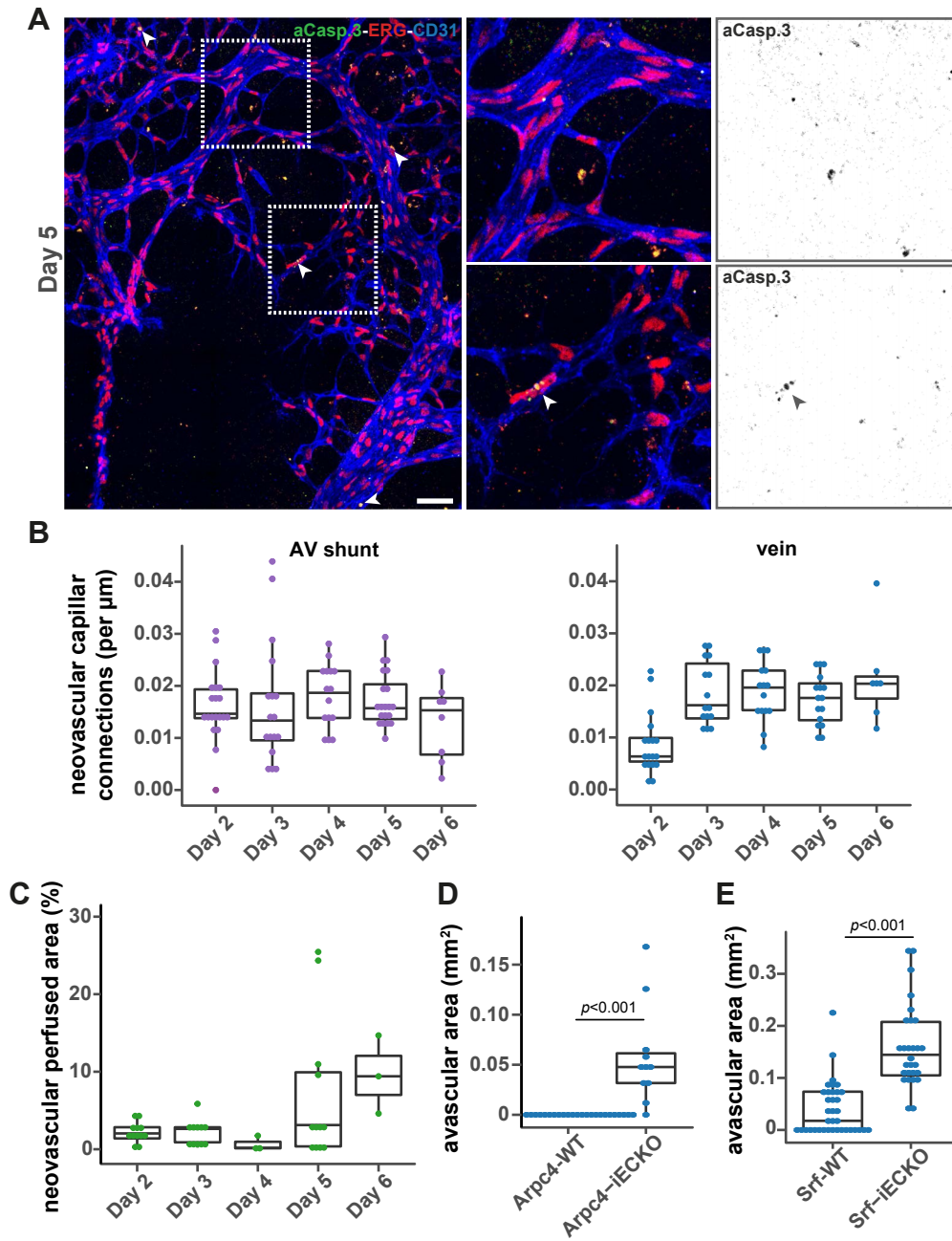
Table 1: Antibodies

Antibody	Conjugation	Manufacturer	Reference	Dilution
cleaved Caspase 3	unconjugated	Cell Signaling	1679664S	1/100
CD31	-	R&D	AF3628	1/200
Donkey anti-Goat	Alexa Fluor 488	Thermo Fisher	A11055	1/400
Donkey anti-Goat	Alexa Fluor 555	Thermo Fisher	A21432	1/400
Donkey anti-Goat	Alexa Fluor 647	Thermo Fisher	A21447	1/400
Donkey anti-Rabbit	Alexa Fluor 488	Thermo Fisher	A21206	1/400
Donkey anti-Rabbit	Alexa Fluor 568	Thermo Fisher	A10042	1/400
Donkey anti-Rabbit	Alexa Fluor 647	Thermo Fisher	A31573	1/400
Donkey anti-Rat	Alexa Fluor 647	Thermo Fisher	A21434	1/400
Desmin	unconjugated	Abcam	ab15200	1/100
ERG	unconjugated	Abcam	ab92513	1/200
ERG	Alexa Fluor 647	Abcam	ab196149	1/75
GFP	FITC	Abcam	ab6662	1/400
Golph4	unconjugated	Abcam	ab28049	1/400
pHistone H3	Alexa Fluor 555	Cell Signaling	3475	1/100
ICAM2	unconjugated	BD Biosciences	553326	1/100
KLF4	unconjugated	R&D	AF3158	1/20
mCherry	Alexa Fluor 594	Alfagene	M11240	1/100
NG2	unconjugated	Merck Millipore	AB5320	1/100
pSmad1/5/9	unconjugated	Cell Signaling	13820	1/100
αSMA	Cy3	Sigma Aldrich	C6198	1/400